Water Research 226 (2022) 119078

Contents lists available at ScienceDirect

Water Research

journal homepage: www.elsevier.com/locate/watres

The key role of surface tension in the transport and quantification of plastic pollution in rivers

Daniel Valero [a,b,*], Biruk S. Belay [c,1], Antonio Moreno-Rodenas [d], Matthias Kramer [e], Mário J. Franca [a,b,f]

[a] Karlsruhe Institute of Technology, Institute for Water and River Basin Development, Karlsruhe, Germany
[b] IHE Delft Institute for Water Education, Water Resources and Ecosystems Department, Delft, the Netherlands
[c] Helmut Schmidt University, Hydraulic Engineering Chair, Hamburg, Germany
[d] Deltares, Hydraulic Engineering Department, Delft, the Netherlands
[e] UNSW Canberra, School of Engineering and Information Technology (SEIT), Canberra, Australia
[f] Delft University of Technology, Rivers, Ports, Waterways and Dredging Engineering Section, Delft, the Netherlands

ARTICLE INFO

Keywords:
Macroplastic
Plastic concentration
Plastic transport
Surfaced plastic
Surface transport
Suspended transport

ABSTRACT

Current riverine plastic monitoring best practices mainly consider surface observations, thus neglecting the underlying distribution of plastics in the water column. Bias on plastic budgets estimations hinders advances on modelling and prediction of plastics fate. Here, we experimentally disclose the structure of plastics transport in surface water flows by investigating how thousands of samples of plastics commonly found in fluvial environments travel in turbulent river flows. We show for the first time that surface tension plays a key role in the transport of plastics since its effects can be of the same magnitude as buoyancy and turbulence, therefore holding a part of the dispersed buoyant plastics captive by the water surface. We investigate two types of transport; surfaced plastics (surface tension-turbulence-buoyancy dominated), in contact with the free surface, and suspended plastics (turbulence-buoyancy dominated). We prove that this duality in transport modes is a major source of error in the estimation of plastic budgets, which can be underestimated by 90 % following current, well-established monitoring protocols if sampling is conducted solely in the water surface. Based on our empirical findings, we optimize physics-driven monitoring strategies for plastic fluxes in rivers, thereby achieving over a ten-fold reduction of the bias and uncertainty of riverine plastic pollution estimates.

1. Introduction

The presence of plastic polymers in industry products intensified over the past decades (Geyer, 2020), which was also accompanied by growing leakages into the environment (Geyer et al., 2017; Jambeck et al., 2015; Thompson et al., 2009). Geyer et al. (2017) estimated a global 381 million tons/year of plastics production, with 79 % of plastics ending up in landfills or the environment. Meijer et al. (2021) suggested that 0.8-2.7 million metric tons per year are diffusively delivered by rivers into the sea, which is in order-of-magnitude agreement with other studies (Lebreton et al., 2017; Schmidt et al., 2017). The spatial extent of plastic pollution dispersion is unprecedented (Andrade et al., 2021; Napper et al., 2020) as well as its capacity to act as supporting vectors for different hazardous species (Cole et al., 2011; Grossart et al., 2019; Haram et al., 2021; Li et al., 2018). In addition to potential impacts on human health (Jenner et al., 2022; Leslie et al., 2022), other life on land and water can also be impaired by plastic waste (Bergmann et al., 2015; Derraik, 2002; Thompson et al., 2009).

Anthropogenic activities involve large amounts of plastics that can potentially enter the freshwater network (Lechthaler et al., 2020). Given that only a small percentage of mismanaged plastic waste reaches the marine environment (Lechthaler et al., 2020; van Emmerik and Schwarz, 2020), efforts should be put into quantifying the transport and retention in the river catchment. Rivers, undeniably, can enable fast and far reaching conveyance of plastics, hence serving as *highways* of plastic litter pollution. However, little is known about detailed transport mechanisms within built and natural water networks (Waldschläger et al., 2022). Plastics in rivers can be observed

* Corresponding author at: Karlsruhe Institute of Technology, Institute for Water and River Basin Development, Karlsruhe, Germany.
E-mail address: daniel.valero@kit.edu (D. Valero).
[1] Previously: IHE Delft Institute for Water Education, Water Resources and Ecosystems department; Delft, the Netherlands.

https://doi.org/10.1016/j.watres.2022.119078
Received 24 May 2022; Received in revised form 6 September 2022; Accepted 7 September 2022
Available online 28 October 2022

travelling well within the water column (herein, *suspended*) or afloat at the free surface (*surfaced*). However, river surveys frequently sample plastics only at the free surface (Geraeds et al., 2019; Kataoka and Nihei, 2020; van Emmerik and Schwarz, 2020; Vriend et al., 2020), thereby enclosing considerable uncertainty and systematic biases since they overlook a great part of the water column (Cowger et al., 2021; van der Wal et al., 2015).

Most exhaustive studies conducted on plastic hydrodynamic mechanisms have focused on quiescent water conditions (Waldschläger et al., 2020; Waldschläger and Schüttrumpf, 2019). Only Zaat (2020) has addressed plastics transport in a turbulent flow under laboratory conditions, but suspension was assumed to be the only mode of transport in the water column, thus not addressing distinctive mechanics of surface transport. Detailed knowledge on plastic-water dynamics is still scarce and may prevent accurate prediction of the fate of plastics in riverine environments under different fluvial conditions.

In this study, we identify and characterize a near-surface layer in which surfaced transport (namely, plastics protruding the free surface), coexists with a modulated suspended transport. We statistically infer, for the first time, that suspended transport in the remaining water column can be explained by classic suspended-particle theories (likewise natural sediments, see Cowger et al., 2021; Waldschläger et al., 2022; Zaat, 2020), whereas we describe a newly devised –and often dominant– mode of transport occurring at the water surface in which surface tension plays a major role. We reconstruct three-dimensional trajectories at millimeter to sub-millimeter accuracy for over 3,400 macroplastic samples being transported by fluvial-type flow conditions. Finally, we assess the bias and uncertainty of common riverine plastic monitoring best practices and provide strategies that yield over a ten-fold reduction of errors in the quantification of plastic budgets.

2. Theory: plastic transport processes in the upper water column

2.1. Balance of forces

We consider a 3D control volume including a plastic element anywhere in the upper water column and any attached bubbles (Fig. 1). We apply the second Newton's law in the vertical direction for a constant mass control volume:

$$\sum F_z = M\frac{\mathrm{d}u_{p,z}}{\mathrm{d}t} \tag{1}$$

with M the total mass of the control volume (water, air and plastic) and $u_{p,z}$ its instantaneous vertical velocity at a time t. The sum of gravity, turbulence and surface tension forces includes (Crowe et al., 2012; Hohermuth et al., 2021):

$$\sum F_z = F_\rho + F_b + F_w + F_\sigma \tag{2}$$

with F_ρ including the weight and buoyancy forces, F_b the added-buoyancy force given by bubbles attached to the plastic elements, F_w the force due to the plastic element coupling with the water flow, and F_σ the surface tension force occurring in the plastic-water-air contact line when the plastic protrudes the water surface. For the water-plastic coupling, we assume that the drag force is a reasonable approximation ($F_w \approx F_D$, see Appendix A). Other forces could be considered in Eq. (2) (Crowe et al., 2012; Hohermuth et al., 2021), but are deemed less relevant under steady flow conditions in the upper water column. Detailed expressions for the forces of Eq. (2) are presented in Appendix A.

2.2. Ratios of dominant forces

Depending on which forces dominate the force balance, different transport regimes may be expected. The most commonly studied mode of particles transport is suspension, which is explained by the ratio of buoyant to turbulent forces. It is well established that small particles in suspension are driven by the ratio of buoyancy and turbulence forces, which can be expressed by the Rouse number (Rouse, 1961):

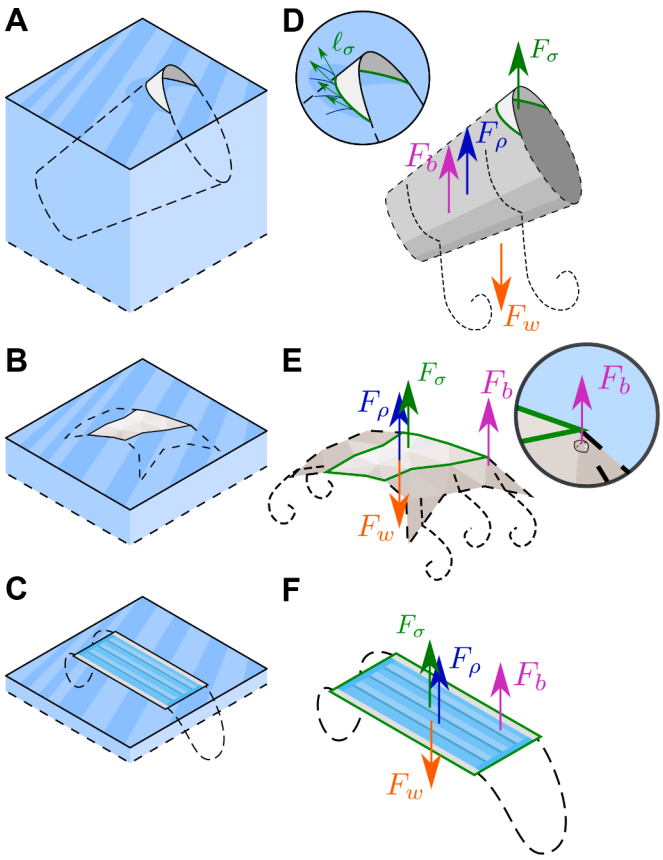

Fig. 1. Forces driving the transport of plastics in river flows. Elements considered: **A** plastic cup, **B** plastic film, **C** face mask; **D, E** and **F** for the representation of the forces acting in the corresponding plastic element.

$$\beta = w/\kappa u_* \tag{3}$$

with w being the rising velocity of the suspended particles (or the settling velocity, for sediments), κ (= 0.41) the von Kármán constant and u_* the flow shear velocity. The parameter β determines the shape of the Rouse profile, which is a theoretical profile for suspended particles in turbulent water flows under the assumption of parabolic and symmetric eddy diffusivity distribution across the water column (Eq. 245 of Rouse, 1961):

$$\frac{C}{C_a} = \left(\frac{1-\eta/\eta_0}{1+\eta/a}\right)^\beta \tag{4}$$

where C_a is the concentration at a reference level a (> 0) below the free surface, or above the channel bed for settling particles, and η the distance starting at the level a in downwards direction (for rising particles, and upwards for settling particles); C is the suspended concentration and η_0 the distance from the level a to the channel bed (or to the free surface for settling particles). For positively buoyant plastics and downward η, the rising velocity is positive and hence $\beta > 0$. Here, we used quiescent transport experiments repeated three times to determine w for each plastic sample considered. In sediment transport, β may also be used to determine the dominant mode of sediment transport; for instance (see Table 1 of Cowger et al., 2021; and Eq. 5.1c, p. 262 and p. 403 of Dey, 2014): bed load, suspended load ($\beta < 1.5$ to 2.5) and wash load ($\beta < 0.8$). Eq. (3) (and Eq. (4)) consider a turbulent Schmidt number of 1 (i.e., turbulent momentum diffusivity equal to the turbulent mass diffusivity,

see Gualtieri et al., 2017; and Eq. 3 of Waldschläger et al., 2022).

Bubbles attached to the plastic particle can represent an additional source of buoyancy, and thus the total buoyancy may be better expressed as $F_\rho + F_b$. Provided that w is determined from rising/settling velocities of particles in quiescent water, attached bubbles may also be present, similar to the transport in turbulent flows. Therefore, it is here assumed that β is representative of the total buoyant force. This also implies that experiments in quiescent flows to determine w should be comparable to the protocols used for turbulent transport testing. In Appendix A and Appendix B, we show that bubbles attached to the plastic samples cannot explain the surface concentrations observed in experiments. Since the contribution of bubbles to the total buoyancy commonly remains at least one order of magnitude smaller than the buoyancy or surface tension (Appendix B, based on laboratory observations of bubbles attachment), F_b is disregarded in the following.

Another relationship of forces can be expressed as the ratio of surface tension (explained by the vertical projection $[\sin\theta]$ of the surface tension σ acting over the air-water-plastic contact line length ℓ_σ) to turbulent forces (due to the turbulent drag of water with density ρ_w, explained by a relative velocity difference $\Delta\mathscr{U}$, a drag coefficient C_D and a plastic area exposed A). Differently from buoyancy, this is only active in the upper layer of the concentration profile and when the plastic element protrudes through the water surface (Appendix A):

$$\frac{F_\sigma}{F_D} = \frac{\ell_\sigma \sigma \sin\theta}{\frac{1}{2}\rho_w C_D A\, \Delta\mathscr{U}|\Delta\mathscr{U}|} \tag{5}$$

We assume that ℓ_σ can be expressed by the two main orthogonal dimensions $\ell_{\max}$ and $\ell_\perp$ (maximum main axis of a particle, and its orthogonal counterpart, see Materials and methods). This implies:

$$\ell_\sigma \approx 2(\ell_{\max} + \ell_\perp) \tag{6}$$

We further assume that the contact angle vertical projection may remain constant across the interfacial contact line, and the following term will be approximated as $\sin\theta \approx \sin 30 = 1/2$. For the drag forces (Appendix A), we also assume that the vertical transport (drag) will be driven by turbulent fluctuations, and consequently:

$$\Delta\mathscr{U}|\Delta\mathscr{U}| \sim u_*^2 \tag{7}$$

The drag coefficient is however variable, and Reynolds dependent, and different plastic element geometries may show different plastic-water coupling. However, we assume here a representative value of $C_D \approx 0.5$. The area of the particle projected in the direction of the dragging flow can be expressed as a fraction (f_A) of the area enclosing the object, which can be written as:

$$A = f_A\ (\ell_{\max} \cdot \ell_\perp) \tag{8}$$

where f_A may depend on the shape and deformability of the object. For the sake of simplicity, we assume a representative value to be in the order of $f_A \approx 0.5$. Bringing together Eq. (5) to Eq. (8), a ratio for the surface tension to turbulent forces acting on a particle can be introduced, which takes a form similar to an inverse (plastic-based) Weber number:

$$\Gamma = \frac{\sigma(\ell_{\max} + \ell_\perp)}{\left(\frac{1}{2}\right)^3 \rho_w (\ell_{\max} \cdot \ell_\perp) u_*^2} = \frac{8\sigma}{\rho_w u_*^2} \frac{(\ell_{\max} + \ell_\perp)}{(\ell_{\max} \cdot \ell_\perp)} \tag{9}$$

In Eq. (9), the numerator is proportional to the interfacial contact line whereas the denominator increases with the area of plastic exposed to turbulence. This implies that surface tension effects become more important (greater Γ) when the element is small, or the flow velocity decreases. Besides, although not captured in Γ, plastics with a corrugated shape (or high fractal dimension) would represent larger interfacial contact lines than considered in Eq. (9), thus subject to a stronger surface tension influence. Appendix A also presents the derivation of a plastic-based Bond number (buoyancy to surface tension ratio), but we deem more convenient to present the results based on β and Γ since buoyancy and surface tension both act in the same direction in this study.

3. Materials and methods

3.1. Experimental setup

Experiments were conducted in the Hydraulic Engineering Laboratory of the Delft University of Technology. The plastic turbulent transport experiments took place in a rectangular flume (Fig. 2A-E), with main dimensions: 14.40 m long, 40 cm deep, 40 cm wide, and bed slope

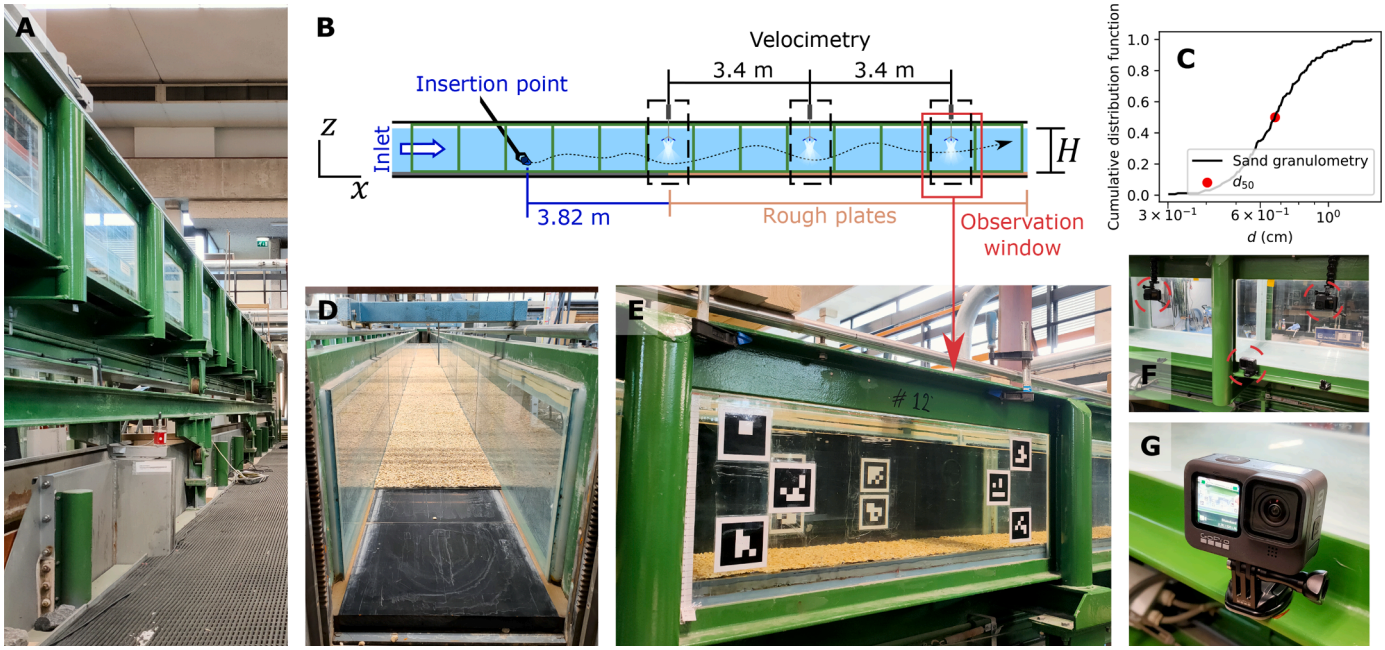

Fig. 2. Experimental flume. **A** Side view, **B** sketch and main dimensions, **C** granulometry of the sand plates (and median grain size, d_{50}), **D** channel view from downstream (dry channel), **E** observation window and ArUco markers for automatic camera referencing, **F** front cameras arrangement and **G** fixation of a frontal camera. Front cameras are fixed in a different, side channel (1.53 m apart), and are separated 34 to 43 cm from the central one. Upper cameras (**F**) are at the free surface level (H).

Table 1
Flow conditions in the experimental setup. Total discharge (Q), uncertainty in its estimation (ε_Q), specific discharge (q), Froude number ($F = U/\sqrt{gH}$, with U the depth-averaged velocity), and Reynolds number ($Re = 4q/\nu$, with ν the water kinematic viscosity). Shear velocity u_* and boundary layer thickness δ correspond to a log-wake law profile fit. Shear velocity $u_{*,\tau}$ and boundary layer thickness δ_τ correspond to a Reynolds shear stresses linear profile fit.

ID	Q (m^3/s)	ε_Q (%)	q (m^2/s)	H (m)	U (m/s)	F (-)	Re (-)	u_* (m/s)	$u_{*,\tau}$ (m/s)	δ (m)	δ_τ (m)
V1	0.035	3.21	0.088	0.278	0.318	0.193	353,768	0.0213	0.0174	0.111	0.120
V2	0.053	1.80	0.132	0.278	0.475	0.288	528,405	0.0320	0.0285	0.116	0.121
V3	0.073	2.34	0.183	0.278	0.657	0.398	730,843	0.0444	0.0388	0.105	0.120
V4	0.088	2.49	0.219	0.278	0.787	0.477	875,200	0.0535	0.0484	0.106	0.103
V5	0.100	2.24	0.251	0.278	0.901	0.546	1,002,458	0.0613	0.0555	0.102	0.105

estimated at 0.00026. A 9.58 m long rough bed was installed to enhance turbulence in the flow. The rough plates included closely packed sand grains with median diameter of 0.67 cm. The granulometry curve is also included in Fig. 2C for completeness.

Rising tests were conducted in a separate flume to characterize the rising velocity of the plastic samples under quiescent conditions. The samples were introduced with a long grabbing arm and were released after the water surface seemed undisturbed. For this test phase, a static water tank was prepared in the middle of a horizontal flume after closing both ends with wood boards and water-proofing both ends. The dimensions of this water tank are 84 cm in depth and 77 cm width with over a meter in length. A wooden frame was used to position four GoPro HERO9 cameras and record the rising process of the introduced samples. Velocities were obtained at 10 different levels during the rising process and tests were repeated three times.

3.2. Flow hydrodynamic characterization

Five different flow conditions are considered in the plastic transport experiments. These discharges are used for all plastic classes considered in the experiments. All discharges represent subcritical flows with high Reynolds number (Table 1). Water levels in the flume were controlled by a downstream gate. The flow depth was both estimated in the flume with a point gauge for each experiment, obtaining a mean value of 0.278 m (+/- 1 mm, gauge resolution). Several camera recordings were analyzed obtaining a mean water depth of 0.278 m (+/- 1.2 mm, as STD of 10 estimations).

The flow characterization is carried out through velocity measurements at 2 cm vertical intervals using an Acoustic Doppler Velocimeter (ADV, Vectrino +, Version 1.24.00) and upstream hydrogen bubble seeding (Blanckaert and Lemmin, 2006). Each point was sampled for at least 2 minutes, which was determined as long enough recording based on preliminary longer samplings. The sampling frequency was adjusted between 100 and 200 Hz, and transmit lengths between 1.8 and 2.4 mm, depending on local signal quality. Each ADV time series was analyzed following the protocol of Appendix C.

The water discharge was obtained by fitting a theoretical velocity profile (log-wake law and potential flow outside of the boundary layer) to the water velocity measurements and integrating them using a trapezoidal rule (from bed level to water surface). This was done for all five discharges in three different cross-sections (Fig. 2B), with the farther downstream cross section sampled twice – the latter time with 1 cm vertical resolution to assess sensitivity to vertical spacing in the measurements. This resulted in roughly identical discharge estimations. Several, redundant estimations of the discharge at different cross-sections allowed estimating an uncertainty level for this variable (ε_Q, 100·STD/mean of 2.4 %).

3.3. Plastic samples

We consider different clean, positively buoyant macroplastic samples for the water transport experiments (Fig. 3 and Table 2). These are selected to be representative of riverine plastic litter observations while including different mechanical properties: i) rigid 3D objects (cup-shaped, Fig. 3A-D), ii) (quasi–)2D rigid fragments (Fig. 3E-F), iii) plastic bag films (Fig. 3G-J) and iv) face masks (Fig. 3K-M). Samples iii and iv are subject to deformations by hydrodynamic stresses and, when inserted in a turbulent flow, the plastic elements buckle and warp (Fig. 3H,J,L,M).

According to observations of van Emmerik et al. (2020), samples i-iii belong to the 20 most widely found plastic elements in the Rhine-Meuse delta riverbanks and are also representative of previous monitoring campaigns in Asia (van Emmerik et al., 2018). Masks are also considered in our study given their sudden increase in the pollution share experienced during the COVID-19 period (80-fold observed increase of masks in litter, according to Roberts et al., 2021). Further characteristics of the samples used in the experiments are presented in Appendix D.

Materials composing the experimental samples include: Polypropylene (PP, for cup samples) and High-Density Poly Ethylene (HDPE, for films). A material common in riverine litter not directly considered here is Expanded Polyestyrine (EPS). Given its low density (between 0.016 to 0.640 g/cm^3, following van Emmerik and Schwarz, 2020), similar buoyant characteristics may be expected for the masks. By size, all samples can be categorized as *macro* (under all classification frameworks, see Hartmann et al., 2019), which is the dominant category by weight in plastic pollution (Eriksen et al., 2014). All face masks contain porous materials and were submerged for 72 hours prior to testing.

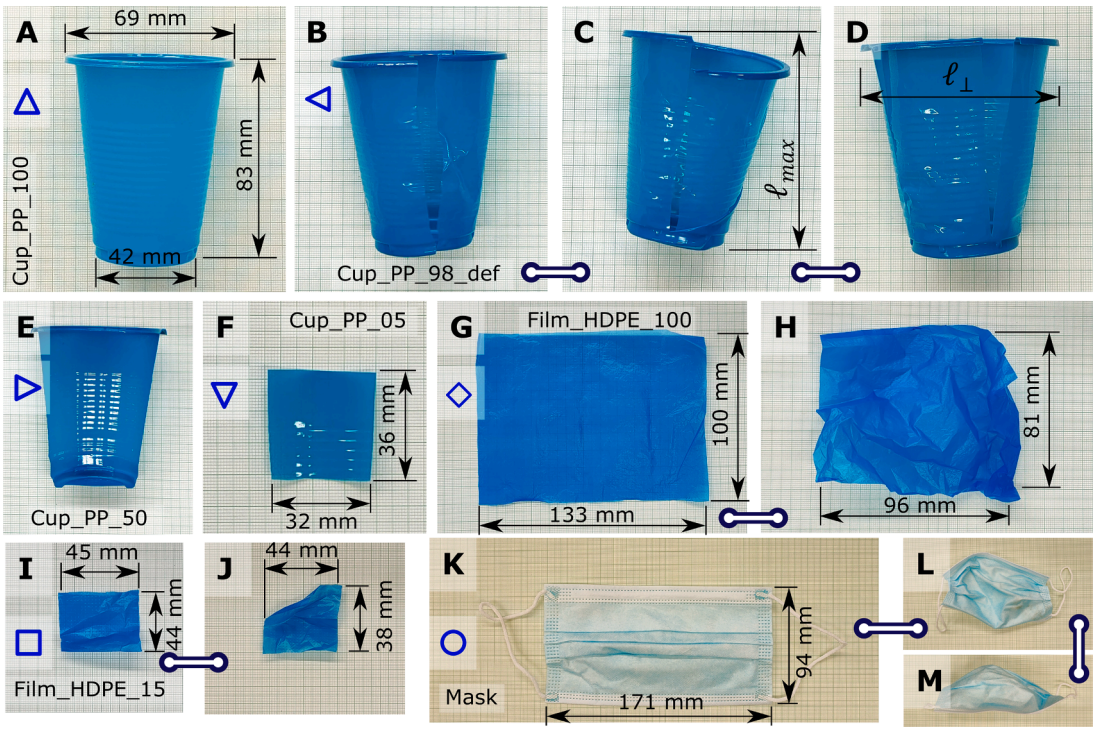

Fig. 3. Samples considered in the transport experiments, main dimensions, IDs and markers used in the upcoming figures. **A** Unbroken polypropylene (PP) cup, **B-D** three selected broken/deformed PP cups, **E** half PP cup, **F** quasi-2D fragment (5 % volume of the whole cup), **G** unfolded piece of deformable High Density Poly Ethylene (HDPE) film, **H** creased piece of HDPE film, **I** smaller piece of HDPE film, **J** smaller creased piece of HDPE film, **K** intact face mask and **L-M** creased face mask. Dimensions correspond to an ensemble averaged estimation.

Table 2
Geometrical properties of the plastic samples used in the hydrodynamic experiments (Fig. 3). ℓ_{max} for the length of the maximal main dimension, $\ell_{\perp}$ for the length orthogonal to the maximal main dimension. ΔV_p: reduction of volume compared to the largest class particles (i.e., _100) and ρ_p the density of the material. The rising velocity w is the result of an ensemble average of the terminal velocity of three experiments (Table D3).

ID	Material*	Class	ℓ_{max} corresponds to	ℓ_{max} (mm)	$\ell_{\perp}$ corresponds to	$\ell_{\perp}$ (mm)	V_p (mm^3) **	ΔV_p (%)	ρ_p (kg/m^3)	w (mm/s)
Cup_PP_100	PP	Rigid 3D body	Height	83	Diameter	69	2303.46	100	907.33	26.2
Cup_PP_98_def	PP	Damaged rigid 3D body	Height	88***	Diameter	72***	2248.36	97.61	907.33	29.2
Cup_PP_50	PP	Rigid quasi-2D fragment	Major side	83	Diameter	69	1146.22	49.76	907.33	18.6
Cup_PP_05	PP	Smaller rigid quasi-2D fragment	Major side	36	Chord	32	121.23	5.26	907.33	11.7
Film_HDPE_100	HDPE	Deformable film	Major side	133	Minor side	100	230.01	100	956.48	5.4
Film_HDPE_15	HDPE	Smaller deformable film	Major side	45	Minor side	44	24.50	15	956.48	2.4
Mask	Several	Deformable multi-layer material	Width	171	Height	94	-	100	-	101.8

* Material determined based on the recycling codes found in the samples and cross checked against common density range for such materials.
** Volume estimated from mass and density of Table D1.
*** As an ensemble of several samples, see Table D2.

3.4. Plastics characterization

Three different sources of plastic elements were considered to produce the plastic elements' samples: plastic cups, plastic films (supermarket bags), and disposable face masks (Fig. 3). These three types of sources were manipulated to generate different plastic *classes*. These are presented in Fig. 3, Table 2 and Appendix D. The densities of prepared plastic samples are tested using a 50 ml pycnometer in the Deltares Geolab. For this, distilled water was used as an immersion liquid (997.98 kg/m^3 at 21°C, estimated using the same pycnometer). From each sample, small fragments are prepared to allow insertion into the pycnometer and carry out the measurements. The density of these samples was tested and estimated according to the specifications of ISO 1183-1:2019(E) for pycnometer tests (ISO, 2019). Each density estimation was repeated 5 times, thus allowing estimation of the method's uncertainty (Appendix D). The samples' material was determined based on the recycling codes found in the packaging, which showed a good match with the expected density's range of each material and that here determined.

The plastic cups included size classes ranging from original form to fragmented parts, including full 3D objects and quasi-2D fragments. In addition, manually damaged cups are also included in these sample groups (crashed against the floor using human weight). Size classes of rectangular plastic films are similarly prepared after cutting out the handles of procured shopping bags, hence obtaining near-rectangular objects. Size measurements and rising velocities are presented in Table 2 and Appendix D.

3.5. Insertion protocol

The insertion point is set at the beginning of the experimental flume (Fig. 2). The plastic sample is carefully introduced inside the water using a 1.5 m long grabbing arm. The newly submerged sample is either

cleared from bubbles by hand (deformable plastics) or shaken 3 times (for rigid samples) while impacting the grabbing arm against the flume's metal structure. This prevents most of the bubbles from remaining attached to the plastic body, although a few may remain yet their contribution to buoyancy is deemed negligible, as we discuss in Appendix B. The sample is released after holding it still with the grabbing arm for 5 seconds at around 20-30 % of the water depth (H).

The number of samples tested was designed based upon a combined Monte Carlo analysis and a two-sided Kolmogorov–Smirnov (KS) test (Appendix E), analyzing the expected difference between a Rouse profile sampled with a limited number of particles N from a reference *true* Rouse suspended-transport concentration profile (Eq. (4)). Therefore, $N = 150$ was set as target for each experiment, although some samples were lost during transport (stuck in the channel glass, for instance) or may remain undetected.

3.6. 3D tracking of the plastic samples

Four GoPro HERO9 cameras were used to record the macroplastic samples at the downstream section of our test flume (Fig. 2B). Three cameras were placed in a vertical plane in front of the observation window (Fig. 2F), and one camera was placed on a wooden frame over the top of the flume, allowing a top view of the free surface. The camera distortion (radial-tangential model) and intrinsic camera parameters were calibrated using 15 images of a chess calibration board at different orientations. To overcome possible changes of camera orientation throughout the measurement campaign, fiduciary markers (ArUco markers, see Garrido-Jurado et al., 2014) were used to continuously reconstruct the relative position of the cameras (see Fig. 2E and Supplementary Material). Cameras recorded at 60 frames per second and were initiated by a common IR remote trigger. An external flash-light was used to perform cross-camera time-synchronization. All cameras used a Sony IMX677 CMOS sensor.

An automated detection routine was built to delineate the macroplastic element contours per frame from the cameras' video sequence. This is based on a background subtraction, an HSV color-space filter and different topological filters based on the expected shape and size of macro-plastics. The script was developed using the OpenCV Python library (Bradski, 2000). A stereo-camera configuration was used to reconstruct the 3D location of the suspended object. First, the detected object centroid is transformed from camera-coordinates to real-world coordinates (intrinsic and extrinsic transformations); secondly, the ray-refraction at the air-to-water phase change is estimated (see Duinmeijer et al., 2019). The minimum crossing distance between the stereo-rays is used to estimate the 3D location of the detected object within the water channel. The point reconstruction error was estimated by comparing the estimated 3D location (from the stereo-camera system) and the measured position of the inside-channel ArUco markers (Suppl. Mat., Table S5).

Additionally, Camera 1 was used to automatically classify macroplastics that are transported in a suspended manner and those attached to the water surface. In each frame, the plastic perimeter is identified and its Center of Gravity (C.o.G.) estimated. A plastic element with at least one point-pixel of the perimeter in contact with the free surface is considered a surfaced plastic. To this end, Camera 1 was carefully placed such that the view is aligned with the channel water surface plane.

4. Results

4.1. Open channel flume hydrodynamics

Plastic transport experiments were conducted in a laboratory flume under five fully controlled flow conditions (Table 1) and strict plastic insertion protocols. Instantaneous flow velocities were sampled for the five flow conditions (Table 1) across three different sections in an experimental rough-bed flume (Fig. 2). The flow reproduced in the flume features a boundary layer, which is the most common flow present in rivers (Franca et al., 2021). In Fig. 4, we show that our open channel flow follows classic theories for canonic river turbulence (downstream cross-section, in the observation window, see Fig. 2B): the mean velocity profiles closely follow a log-wake law with conventional log-wake law parameters and Reynolds normal stresses profiles following the expected decay with increasing distance to the wall. Further to the water hydrodynamics in the plastic observation window (Fig. 4), we also present

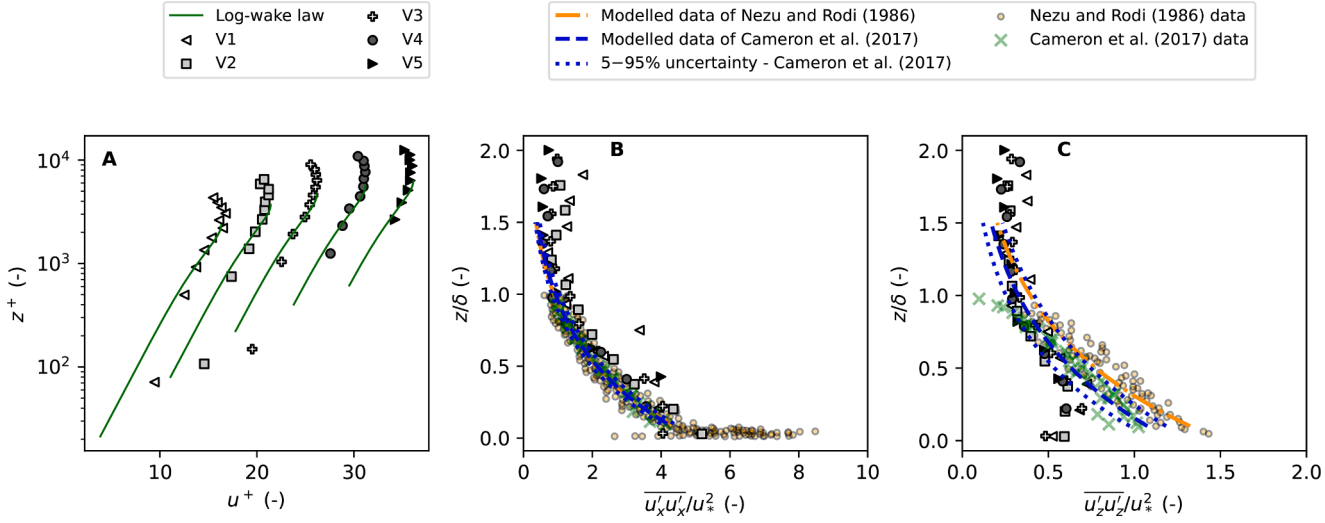

Fig. 4. Water flow hydrodynamics at the plastics observation window (end of flume, 11.6 m from inlet, see Fig. 2B). **A** Mean streamwise velocity (separated by $u^+ = 5$ units for the sake of clarity), **B** streamwise normal Reynolds stresses ($\overline{u_x'u_x'}$) and **C** vertical normal Reynolds stresses ($\overline{u_z'u_z'}$), both normalized by u_*. z^+ is the dimensionless distance to the wall ($z^+ = zu_*/\nu$, with z the distance to the wall and ν the water kinematic viscosity), u^+ is the mean streamwise flow velocity divided by u_*. For reference, the model of Nezu and Rodi (1986) is also adjusted to the data of Cameron et al. (2017) ["modelled data"], together with 5-95 % uncertainty bounds.

mean and turbulent flow quantities at an upstream location in the Supplementary Material (Fig. S1).

Our sampled mean velocity profiles at all cross-sections follow a log-wake law as expected for a boundary layer flow (see Eq. (1) of Castro-Orgaz, 2010). We use default parameters from literature for the log-wake profile (Castro-Orgaz, 2010; Nezu and Rodi, 1986), including the recommended values of Castro-Orgaz (2010); i.e., 8.5 for the constant of integration, 0.2 for the wake strength parameter, and 0.41 for the von Kármán constant (κ). Sand roughness was assumed as the value obtained through imaging of the roughness plates. With these parameters fixed, we obtain the boundary layer thickness (δ) and the shear velocity (u_*) using a least squares procedure. In order to cross-verify the turbulence quantities obtained, we obtain the Reynolds shear stress $\overline{u_x' u_z'}$ profile, which is then used to estimate the shear velocity ($u_{*,\tau}$) and the boundary layer thickness (δ_τ). We do so by fitting a line via the Siegel slopes method (median slope across point-pairs), which is a robust alternative to error-reducing line fitting. The zero-crossing of this line allows direct estimation of $u_{*,\tau}$ and δ_τ.

With the fit of the mean velocity profiles, and assuming a uniform velocity out of the boundary layer upper edge, we numerically integrate the profile to obtain the specific discharge (q). Predictions of the discharge across different cross-sections is in good agreement and differences in the estimation of the shear velocity (between both methods used: mean velocity and turbulent shear stress) are minor, which suggests that low uncertainty is held in our hydrodynamic estimations.

4.2. Thickness of the surface tension-dominated transport

The Centers of Gravity (C.o.G.) of plastics and their trajectories are estimated based on synchronous multi-camera detection and reconstruction (Fig. 5A-B). All the detected plastics in contact with the water surface are classified as surface transport. All surfaced plastics' C.o.G. are confined into a layer of thickness a in the near-surface region, which is here defined as the deepest point at which a surfaced plastic's C.o.G. is detected.

We observe that the near-surface region thickness (a) depends on the plastic elements travelling orientation, which is either driven by: i) turbulence ($\beta\downarrow$) or ii) buoyancy ($\beta\uparrow$); and it is however not affected by surface tension (i.e., Γ-independent). Hence, estimations of a values show a bimodal distribution, each related to one of these two regimes (i and ii). Plastics subject to intense turbulence (regime i) travel in arbitrary orientations within the water column. When they touch the free surface, the rest of the body is still affected by turbulence. Plastics can either crease or unfold if the mechanical properties allow. Any C.o.G. of a sample can extend up to half of the distance between the two most separated points of a plastic element; i.e., $a = 0.5\lambda$ (Fig. 5E, Appendix F), with $\lambda = (\ell_{\max}^2 + \ell_\perp^2)^{1/2}$.

Nonetheless, with increasing buoyancy (regime ii), samples are pushed up against the free surface. Turbulence may pull the plastic elements downward, but it is insufficient to disturb their transport configuration. Hence, the plastic elements rest against the free surface in a stable, equilibrium position while being conveyed by the free stream flow. The surface transport thickness a in regime ii corresponds to the configuration with minimum potential energy. Accounting for both (i) turbulence- and (ii) buoyancy-dominated regimes, the lower limit of the surface transport layer can be estimated by (a: r^2= 0.59, RMSE= 0.012 m, Median Abs Err = 0.0046 m, Fig. 5E):

$$\frac{a}{\lambda} = 0.36 + 0.14\tanh(3.2 - \beta) \text{ for } 0.2 < \beta < 11.7 \quad (10)$$

To ascertain significance to the existence of a transport layer that differs from turbulent suspension, we conduct a statistical test (specifically, a two-sided Kolmogorov-Smirnov (KS) test, Appendix G). The KS test is iteratively applied to the count profiles of each experiment. This statistical methodology consists on the comparison of the observed vertical distribution of C.o.G. of the plastic elements to a reference suspended transport profile (herein, a Rouse suspended concentration profile (Rouse, 1961), given by Eq. (4). Instead of using best fit parameters (as for instance, Zaat, 2020), the reference Rouse profile is estimated purely based on physical parameters (β): namely, the rising velocity of the samples (Table 2) and the shear velocity of the flow (Table 1).

The KS test is applied to an increasing number of points (Fig. 5F), starting from the sampling point nearest to the channel bed, and gradually moving up until the free surface. When reaching the upper layers of the water column, the experimental observations start differing more significantly from the reference Rouse profile. This deviation of the empirical and theoretical profiles suggests that other physical mechanisms, beyond a turbulent – buoyant force balance, may be driving the concentration in the near-surface layer. For the KS test, a pronounced concavity in the concentration profile is usually marking the lower limit of the surface transport (Fig. 5C and Supplementary Material). This concavity is caused by the missing samples at this level, which might have remained attached to the free surface (Fig. 5C, at $z - H \approx -7.5$ cm, for instance). A second mechanism triggering a significant p-value is due to an overshooting of concentrations close to the surface (Fig. 5D).

We note that a limited number of samples may lead to larger KS stats, although this is well-identified by the p-value. For completeness, we include a Monte Carlo simulation with 85,000 pairs of reference suspended transport profiles in the background of Fig. 5F, together with median and 5th / 95th percentiles (for a given number of samples). Considering a p-value of 10^{-3}, 73 % of the analyzed concentration profiles show distributions significantly deviating from suspended transport (i.e., solely turbulence/buoyancy-dominated). The depth at which this occurs (a_{KS}, Fig. 5C,D) follows on average terms the thickness a explained by direct identification of the deepest plastic elements in contact with the free surface (Appendix F).

4.4. Transport of plastics in the near-surface

The total number of plastic elements detected in one experiment at a given cross-section is here denoted as N_p and is made of the particles in the lower suspended transport region (N_β) and the particles in the near-surface region (N_Γ); i.e., $N_p = N_\beta + N_\Gamma$ (Fig. 6A). Within the near-surface layer, we observe plastic elements travelling in suspension ($N_{\Gamma,\text{sus}}$) and surfaced plastics captured by the free surface, and hence affected by surface tension ($N_{\Gamma,\text{surf}}$). A plastic is counted within $N_{\Gamma,\text{surf}}$ when in contact with the free surface. Within the thickness a, but not satisfying the prior condition, the plastic element is counted as $N_{\Gamma,\text{sus}}$. Plastics below the thickness a are all considered part of N_β (Fig. 6 and Appendix F for the full dataset).

The relative frequency of surfaced plastics ($C_{\Gamma,\text{surf}} = N_{\Gamma,\text{surf}}/N_\text{p}$) can be estimated by the following relationship ($C_{\Gamma,\text{surf}}$: r^2= 0.71, RMSE=

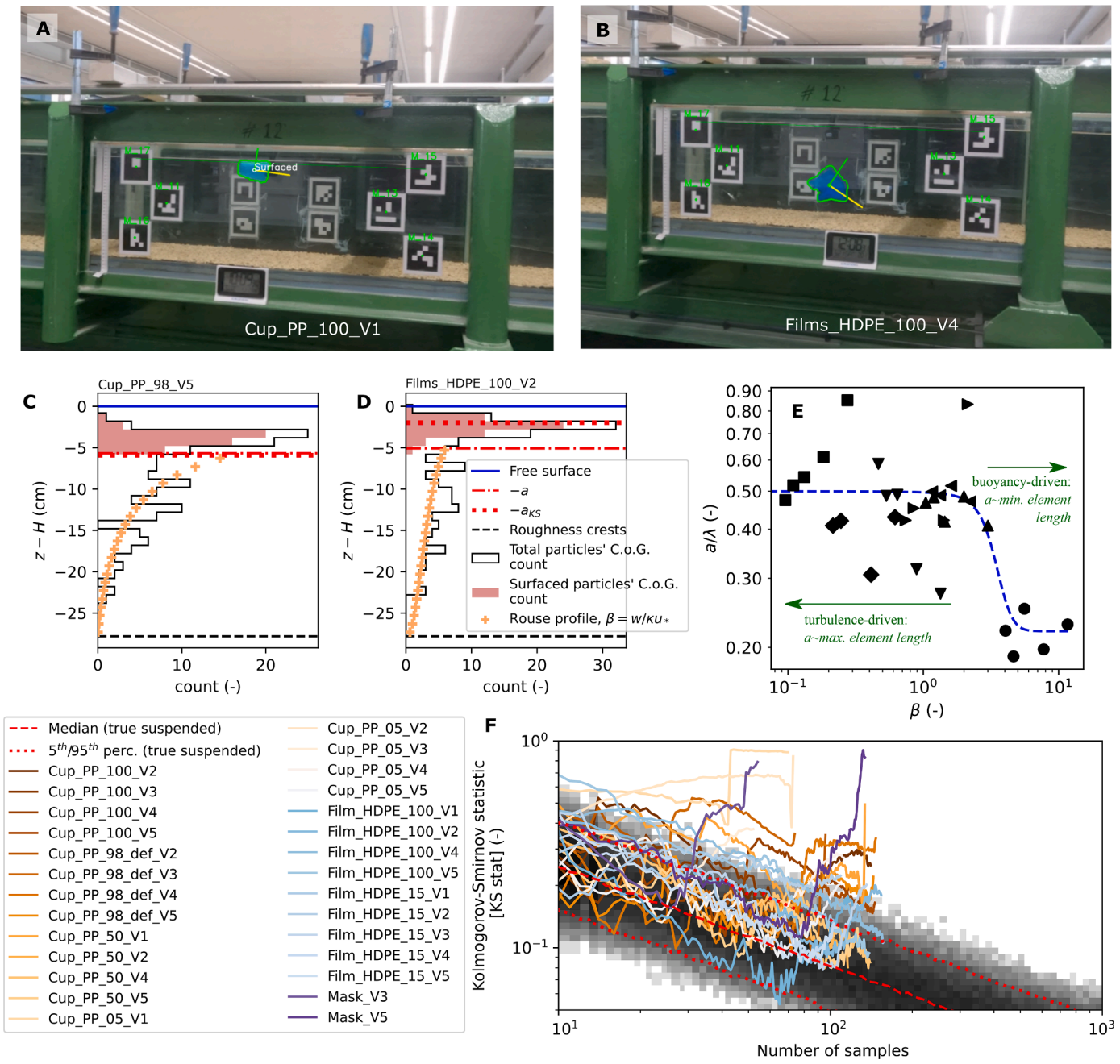

Fig. 5. Suspended and surfaced plastics. Automatic detection of: **A** one surfaced full cup and **B** one film in suspension. **C-D** Concentration profiles for damaged cups and full films. **E** Lower limit of surface transport (markers correspond to the samples of Fig. 3 and dashed line to Eq. (10)). **F** KS stats result for each experiment (with at least 15 samples in suspension, for visualization purposes); increasing number of samples imply depths closer to the free surface, and KS stats out of the 5th / 95th percentiles represent potentially significant deviations from a physically based, true Rouse profile (Eq. (4)).

0.17, Median Abs Err = 0.066, Fig. 6B,D):

$$C_{\Gamma,\mathrm{surf}} = \left[1 + K_{p,0}\left(\exp\left(-\frac{\beta}{\beta_{\mathrm{surf},c}}\right)\cdot\exp\left(-\frac{\Gamma}{\Gamma_{\mathrm{surf},c}}\right)\right)\right]^{-1}, \quad \text{for } 0.2 < \beta < 11.7 \text{ and } 2.5 < \Gamma < 75.1 \tag{11}$$

with $K_{p,0} = 6.66$, $\beta_{\mathrm{surf},c} = 0.64$ and $\Gamma_{\mathrm{surf},c} = 2.37$. Provided that surfaced plastics in the field can be readily observed by direct top-view observation (e.g., from high-resolution satellite data, automated CCTV, or manual counting), Eq. (11) allows an estimation of the expected total plastic count for the complete water column ($N_p = N_{\Gamma,\mathrm{surf}}/C_{\Gamma,\mathrm{surf}}$).

The relative count of plastics in suspension in the lower water column can be explained by the following relationship $C_\beta (= N_\beta/N_p$: $r^2 = 0.75$, RMSE= 0.14, Median Abs Err = 0.067, Fig. 6C,E):

$$C_\beta = \exp\left(-\beta/\beta_{\mathrm{sus},c}\right)\cdot\exp\left(-\Gamma/\Gamma_{\mathrm{sus},c}\right), \quad \text{for } 0.2 < \beta < 11.7 \text{ and } 2.5 < \Gamma < 75.1 \tag{12}$$

with $\beta_{\mathrm{sus},c}$=1.61 and $\Gamma_{\mathrm{sus},c}$= 38.08. If N_Γ is available in a river section, via visual observation or surface sampling with nets, Eq. (12) allows the estimation of the total plastic count following $N_p = N_\Gamma/(1 - C_\beta)$ and may hold lesser uncertainty than Eq. (11). For the sake of completeness, we also estimate the non-stationarity of these estimations by computing the % of change of C_β per unit meter within the observation window (Table F2). On average terms, this amounts to 1.2 %/m (positive and

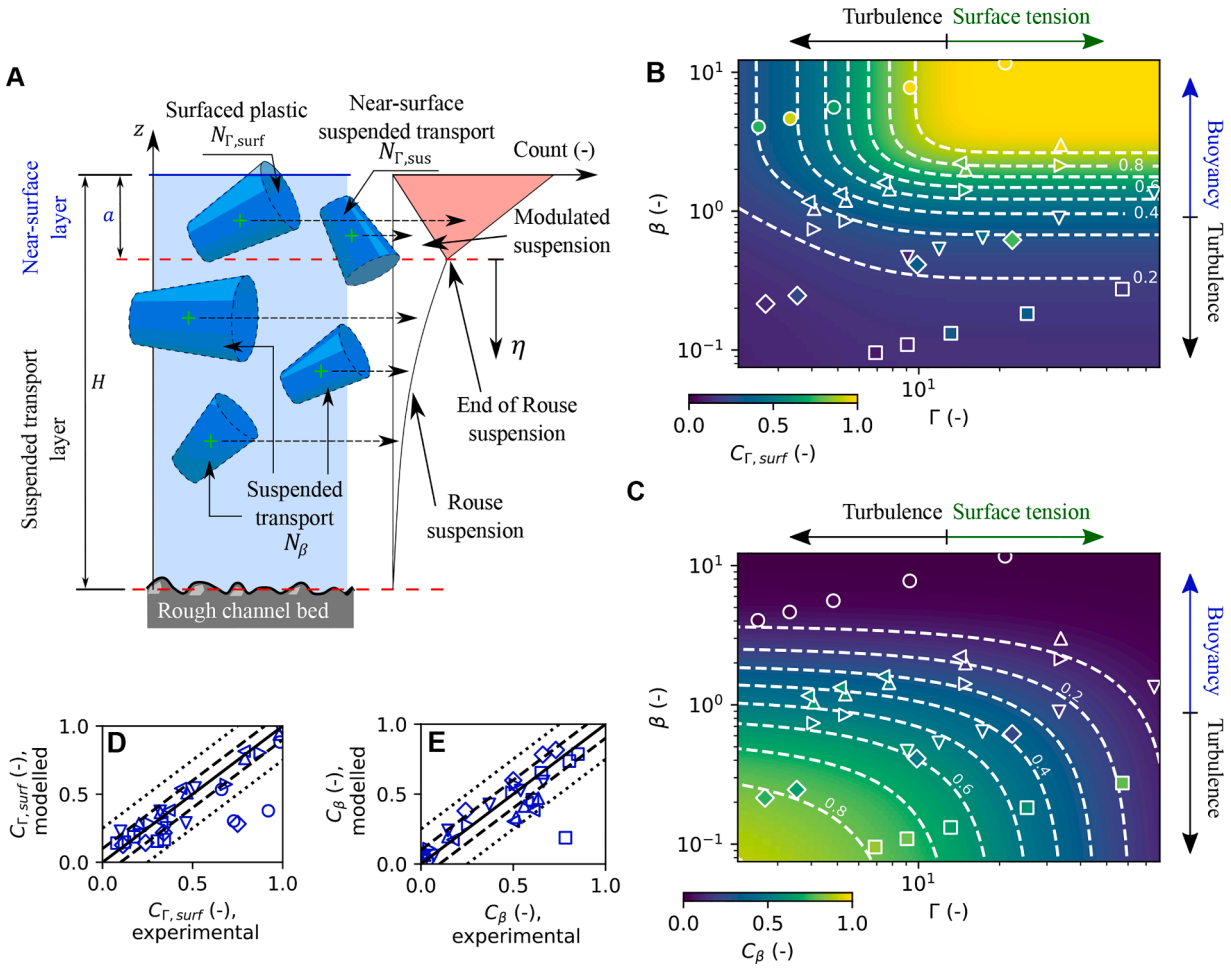

Fig. 6. Surfaced plastics and suspended plastics. **A** Sketch and parameters definitions. **B** Plastics at the free surface, markers for experimental results and color-gradient for Eq. (11). **C** Plastics in the suspended transport layer, markers for experimental results and color-gradient for Eq. (12). **D, E** Deviations between experimental observation and modelled with Eqs. (11) and 12, correspondingly; solid line for 1:1 agreement, dashed lines +/- 0.10 and dotted line for +/- 0.25. Markers correspond to the samples of Fig. 3.

negative tend to compensate), whereas the average absolute value (i.e., expected intensity of the % of change of C_β per unit meter for a random experiment) amounts to (+/-) 8.5 %.

We observe that surface tension effects on the concentration profile can be as intense as buoyancy. For instance, over 90 % of plastics for $\Gamma > 10$ and $\beta > 2$ are travelling as surfaced load (Fig. 6B and Appendix F). Our results suggest that in the near-surface layer, the role of suspension is diminished when compared to the remaining water column (Fig. 5C, D). This modulation of the suspended count may be explained by the reduced number of samples available to travel in suspension after some being trapped at the free surface. Thus, a suspended concentration profile alone cannot explain the near-surface layer (of thickness a) and the lower water region (of thickness $H - a$) together.

5. Discussion

5.1. Plastics monitoring in rivers

Most common methods for the monitoring of plastics in rivers include (van Emmerik and Schwarz, 2020): 1) visual counting using rivers' infrastructure-mounted cameras – or satellite (Topouzelis et al., 2019) — and 2) sampling the flow using nets at different depths. Water surface monitoring, alone or combined with limited net sampling, are standardized monitoring methodologies (González-Fernández and Hanke, 2017; van Emmerik et al., 2018), although they can introduce bias in the total plastic budget (Cowger et al., 2021; van der Wal et al., 2015). In the light of our findings, we assess the bias and uncertainty related to four plastic monitoring strategies targeting the estimation of the plastic budget (N_p^*) in the water column, which reflect both common practices and upgraded procedures herein optimized. Two strategies (Str.) based on common practices are first considered:

- Str. A: the count at the free surface is considered as the estimate of the total plastic ($N_p^* \approx N_{\Gamma,surf}$). The surface count corresponds to floating plastics that emerge through the free surface (surfaced transport), which are detectable independently of the water turbidity levels.
- Str. B: we consider the same monitoring of Str. A but with improved visibility conditions allowing identification of plastics in the upper 20 % of the water column ($N_p^* \approx N_\Gamma$). This strategy assumes favorable visibility conditions in the field, with plastics visually accessible up to a certain depth (for instance, 10 cm in the Saigon river, according to van Emmerik et al., 2018); or the use of nets that allow sampling down to a limited depth beneath the free surface.

Both Str. A and Str. B are currently the common practice for plastics monitoring (González-Fernández and Hanke, 2017; Lebreton et al., 2017; Topouzelis et al., 2019; van Emmerik et al., 2018) and represent pessimistic and optimistic field conditions, respectively. The main inconvenience of these strategies is that they neglect most plastics transported in suspension, which are a significant fraction for $\beta < 3$. For

this reason, we propose two additional strategies:

- Str. C: we expand Str. B by estimating the suspended transport concentration through Eq. (12) ($N_p^* \approx N_\Gamma/(1 - C_\beta)$). This strategy acknowledges the existence of two transport layers and builds on the herein disclosed hydrodynamic behavior of plastics.
- Str. D: we expand Str. B by sampling the suspended transport concentration using nets at a given depth within the suspended transport layer ($N_p^* \approx N_\beta + N_\Gamma$). The sampled suspended concentration is used to infer a physically-based Rouse profile (β-defined), which is integrated over the lower 80 % water column. The suspended sampling location is proposed at 60 % of the water depth based on protocol optimization (Appendix H).

We show that basic monitoring practices, only focusing on the water surface and near-surface (Str. A and Str. B), can underestimate the total amount of plastic by up to 90 % (see Fig. 7) when $\beta < 1$, which is consistent with discussion of van der Wal et al. (2015) and Cowger et al. (2021) regarding the need for sampling plastics in suspension. Str A and B can be a valid practice when the buoyant characteristics of the samples dominate over the flow turbulence ($\beta > 3$).

Distinctly, two different regimes can dominate plastic transport depending on the values of β and Γ. By introducing Str. C (Fig. 7 and Table 3), we show that monitoring one layer while incorporating a point estimation for the plastics in the remaining water column with Eq. (12) leads to over a ten-fold reduction of the bias, and reduces uncertainty by half, when compared to Str. B. Furthermore, Str. D shares the improvement of Str. C in terms of bias but also achieves over a ten-fold reduction of the uncertainty when compared to Str. B, which nonetheless accounts for favorable visibility conditions in the application of a best practices monitoring protocol.

When adopting Str. C or D, two relevant physically-based parameters (the Rouse number β and Γ) are required, which depend on the plastic element and flow conditions. Other optimized monitoring protocols independent of β and Γ, are also presented in the Appendix H together with an assessment of their bias and uncertainty.

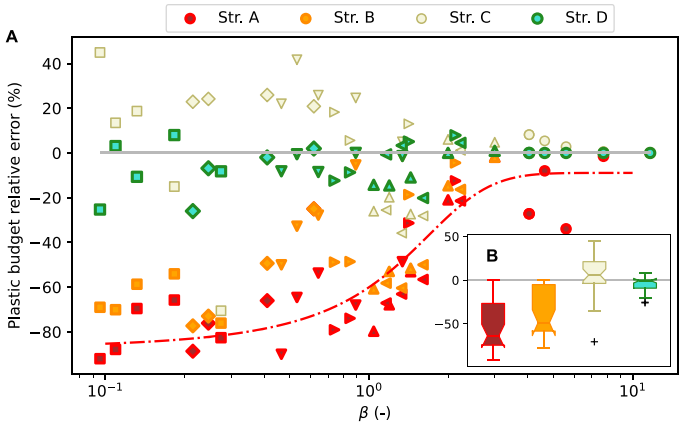

Fig. 7. Relative error of the total plastics estimation for different monitoring strategies (Str). **A** β-dependence (markers correspond to the samples of Fig. 3, red dot-dashed line for Eq. (11) with $\Gamma = 10$, and solid line for null error), **B** box whisker plot for the relative error of different monitoring strategies.

Table 3
Bias (Rel. Mean. Err.) and uncertainty (Rel. Median Abs. Err.) for selected river monitoring strategies.

	Monitoring strategy			
Performance estimator	Str. A	Str. B	Str. C	Str. D
r^2 (-)	0.16	0.25	0.73	0.93
Relative Mean Error (%)	-52.43	-36.16	3.60	-4.51
Relative Median Absolute Error (%)	-63.84	48.71	19.25	4.79

5.2. Implications for plastic removal

We observe that besides buoyancy (plastic-related), the vertical distribution of buoyant plastics is controlled by two other factors: turbulence and surface tension. For instance, river reaches of low turbulence (e.g., $\beta > 2$ and $\Gamma > 10$) can offer an opportunity for efficient cleanup targeting the water surface, since the surface count N_Γ dominates the plastic budget. We also suggest that the free surface collection of plastics may be altered through hydrophobic coating or specific surface treatment of the plastic elements, which can result in a positive impact on removal efforts, although other chemical and toxicological implications should be carefully considered. This can be achieved by targeting an increase of the air-water-plastic contact angle or the interfacial contact line. Contrastingly, the presence of surfactants may impair plastic removal efforts.

6. Conclusions

In this study, we investigated the transport of macroplastics in turbulent river-like flows by using laboratory experiments and physics-based descriptors, which include the ratio of buoyancy to turbulent forces (β) and the ratio of surface tension to turbulent diffusion (Γ). We showed that in the upper water column:

- Two transport regimes can coexist: regime (i), which is driven by the balance between buoyancy, surface tension and turbulence (surfaced transport), and regime (ii), which is driven by the balance of buoyancy and turbulence (suspended transport). We note that, in our experiments, bubbles had a minor effect (Appendix B).
- The near-surface region thickness is defined by the maximum dimension of the plastic elements transported by the flow (Fig. 5E, Eq. (10) and Appendix F).
- Suspended transport did not significantly deviate (in statistical terms) from a physically-based (without calibration) Rouse theoretical suspended transport profile (Eq. (4)), as shown in Fig. 5F. This may hold true for microplastics and smaller size particles, where large-size effects of the plastic particles should be less important. Eq. (3) (and Eq. (4)) were used considering a turbulent Schmidt number of 1 (Gualtieri et al., 2017; Waldschläger et al., 2022). Calibrating this turbulent Schmidt number should allow reducing deviations from the Rouse profile in the suspended transport region (where derivation hypotheses hold true).
- In riverine monitoring campaigns, failing to account for suspended transport can have major implications (Str. A and B, in Fig. 7 and Table 3). This is relevant for small β and large Γ values. When only considering the surfaced plastic budget as representative of the total budget, Eq. (11) can provide an estimation of the missing plastic budget (Fig. 7) or allow an uncertainty estimation related to local flow conditions (captured via β). Our results also suggest that Eq. (12), together with sampling in the near-surface, is a better suited monitoring option (Str. C, in Fig. 7 and Table 3); although two points sampling combined with Eq. (4) still remains more robust (Str. D, in Fig. 7 and Table 3).
- Whereas the top performing monitoring strategy is Str. D (in Fig. 7 and Table 3), additional monitoring strategies are studied in Appendix H. Advantages of these alternative monitoring techniques are the reduced information needed from the plastic elements sampled or reduced sampling efforts.

Funding

Dutch Ministry of Infrastructure and Water Management (Rijkswaterstaat) under MoU scheme with IHE Delft [DV]. Dutch Ministry of Foreign Affairs, Orange Knowledge Programme (OKP), Grant number: OKP-MA.19/00395 [BSB].

CRediT authorship contribution statement

Conceptualization: DV, MJF; Data curation: BSB, DV, AMR; Formal analysis: DV, BSB, AMR; Methodology: DV, AMR, MK, MJF; Investigation: BSB; Visualization: DV; Funding acquisition: DV; Project administration: DV; Resources: DV, BSB; Software: DV, AMR; Supervision: DV, MJF; Writing – original draft: DV; Writing – review & editing: DV, BSB, AMR, MK, MJF

Declaration of Competing Interest

Authors declare that they have no competing interests.

Data availability

All processed data and processing codes are available in the main text, the supplementary material or under: https://doi.org/10.5281/zenodo.7084936 - Raw videos are available upon reasonable request.

Acknowledgments

The authors are grateful to Dr. Hofland, Mr. van der Gaag and Ms. Willems for the support provided in TU Delft Hydraulic Engineering laboratory.

Supplementary materials

Supplementary material associated with this article can be found, in the online version, at doi:10.1016/j.watres.2022.119078.

Appendix A. Hydrodynamic forces over the plastic-centered control volume

The weight-buoyancy force (F_ρ) can be estimated through the Archimedes principle, corresponding to the difference between the weight of the plastic element and the weight of the displaced water, such as:

$$F_\rho \equiv \rho_w g V_b - \rho_p g V_p \tag{A1}$$

with ρ_w being the density of the water, ρ_p the particle density, V_b and V_p the submerged volume and the element's volume respectively, and g ($= 9.81\text{m/s}^2$) the gravity acceleration.

The added-buoyancy force (F_b) can be written as:

$$F_b \equiv \sum_i^{n_b} (\rho_w - \rho_a) g V_{db,i} \tag{A2}$$

with ρ_a the air density, and $V_{db,i}$ the volume of a bubble i (out of n_b total bubbles) of diameter $d_{b,i}$, given by:

$$V_{db,i} = \frac{1}{6}\pi \left(d_{b,i}\right)^3 \tag{A3}$$

The flowing water exerts stresses and pressure over the control volume, which can be defined as:

$$F_w \equiv \oiint \boldsymbol{e}_z \cdot (-p_d \boldsymbol{I} + \boldsymbol{\tau}) \cdot \boldsymbol{n} \, \mathrm{dS} \tag{A4}$$

with $\boldsymbol{e}_z$ ($= [0,0,1]$) the vertical unit vector. Given that the sum of forces is established for the vertical direction z, $\boldsymbol{n}$ ($= [n_x, n_y, n_z]$) the outward vector normal to dS (the infinitesimal element of surface enclosing the 3D control volume), p_d the dynamic pressure (deviation from the hydrostatic component). $\boldsymbol{I}$ is the unit diagonal tensor and $\boldsymbol{\tau}$ the Reynolds stress tensor ($\boldsymbol{\tau} = \tau_{ij}$, with $i,j = x,z,y$). The first term ($-p_d \boldsymbol{I}$) represents the form drag resulting from non-hydrostatic pressure surrounding the plastic element, and the second term corresponds to the Reynolds stress contribution to the drag. Eq. (A4) requires knowledge on pressures and turbulent stresses acting over the control volume surface. Alternative approaches to the flow-plastic interaction include: i) distinguishing between undisturbed flow and disturbed flow forces (See chap. 4 of Crowe et al., 2012) or ii) distinguishing between quasi-steady drag and unsteady forces; i.e., added mass and Basset forces (see chap. 4 of Clift et al., 1978). The undisturbed flow considers changes in pressure and velocities of the flow due to reasons exogenous to the element itself (for instance, local accelerations in a contraction), and hence depend on the water flow through the channel. For the disturbed flow forces, an integral approach is based on the use of a (quasi-)steady drag (F_D) approach, which can be brought together with the following unsteady forces, the added mass force (F_{vm}) and Basset force (F_B):

$$F_w \equiv F_D + F_{vm} + F_B \tag{A5}$$

Considering an integral approach, and disregarding unsteady forces:

$$F_w \approx F_D \tag{A6}$$

For the quasi-steady drag (F_D), we consider that the plastic particle is dragged by a velocity difference between the instantaneous water and particle velocities ($\Delta\mathscr{U}$):

$$F_D = \frac{1}{2}\rho_w C_D A \, \Delta\mathscr{U}|\Delta\mathscr{U}| \tag{A7}$$

with C_D the drag coefficient (commonly obtained empirically in quiescent water conditions, i.e.: free falling or free raising particles) and A is the frontal area of the object.

When a plastic element is only partly submerged, an air-water-plastic contact line exists. In this interfacial contact line, the free surface bends, thus leading to a vertical component of the surface tension force (see Fig. 1D). The surface tension force can be expressed in terms of the capillary action

over the interfacial contact line (White, 2016):

$$F_\sigma \equiv \oint \sigma \sin(\theta)\ \mathrm{d}\ell \approx \ell_\sigma\ \sigma \sin(\theta) \tag{A8}$$

with σ (= 0.073 N/m) the surface tension (White, 2006), and $\sin(\theta)$ accounts for the vertical projection of the force and $\mathrm{d}\ell$ is a differential segment in the interfacial contact line. Eq. (A8) assumes that surface tension has an equally distributed effect over the contact length ℓ_σ. The contact angle depends on the air-water-plastic physico-chemical conditions (White, 2016) and the plastic-water-air contact geometry.

The previous equations allow obtaining β and Γ (plastic-based inverse Weber number). A third ratio of relevant forces can be given by the buoyancy to surface tension forces ratio. Both of these forces are acting in the positive direction, but the second one is only present in the upper region of the water column. The maximum magnitude of F_ρ for a buoyant particle occurs when the object is fully submerged ($V_b = V_p$), and thus:

$$\frac{F_\rho}{F_\sigma} = \frac{(\rho_w - \rho_p) g V_p}{\ell_\sigma\ \sigma \sin(\theta)} \tag{A9}$$

Due to experimental constraints, it may arise more feasible to estimate the mass of a plastic element than its volume, and it may thus be convenient to write: $V_p = M/\rho_p$. Following the previous approximations, the ratio between buoyancy and surface tension forces can be expressed as:

$$\Lambda = \frac{(\rho_w/\rho_p - 1)\ gM}{\sigma(\ell_{max} + \ell_\perp)} \tag{A10}$$

which is a plastic-based Bond (or Eötvös) number. A combination of two of the three parameters β, Γ and Λ should suffice to describe the turbulent transport at the free surface. It is here judged convenient to use β, as it is well established and most useful for the study of suspended transport, and use Γ as complementary parameter since it better represents the balance between positive and negative forces —surface tension keeping at upper levels the plastic body whereas turbulence dragging it away from the free surface—, in analogy to β. Furthermore, ρ_p is not available for masks and interpretation of Λ is not straightforward (an increase of Λ means that plastics will be more often in contact with the free surface as well, where surface tension is activated, and a decrease of Λ means that surface tension becomes more intense than buoyancy yet lesser plastics will approach the free surface; besides, both buoyancy and surface tension act in the same direction in this study).

Appendix B. Relative contribution of surface tension, bubbles and buoyancy to plastic dynamics

Surface tension

When plastics protrude the free surface, surface tension acts over the contact line. The contact angle of PP is estimated by Vlaeva et al. (2012) at 97.0 +/- 0.8 ° (at 25°C) while for HDPE de Luna et al. (2014) estimated 96.5 +/- 3.4 ° (at 25°C). Different temperatures or surface treatments can alter the contact angle. For reference, ACCU DYNE TEST (2009b) compiles contact angles from different studies for PP with values commonly ranging between 95 and 117°. For PE (both low and high density PE), ACCU DYNE TEST (2009a) lists values commonly ranging between 93 and 105 °.

Bubbles

Bubbles can be attached to the plastic samples. The insertion protocol leads to the detachment of most of the bubbles, but some may inadvertently remain at the plastic surface. We observed the number of bubbles in 20 different samples (following our insertion protocol) for the following plastic classes (Table 2): Cup_PP_100, Cup_PP_05 and Film_HDPE_15; under the lowest and highest discharges considered in the transport experiments (V1 and V5, see Table 1). We held the plastic samples close to the channel glassed wall without releasing them and we identified the number of bubbles attached to the plastic element. The diameter could not be accurately determined, but it was classified within the following groups: small, medium and large; which roughly correspond to $\ll 1$ mm, ~ 1 mm, and $\gg 1$ mm. The bubbles' counts are presented in the available data. We observe that mainly small bubbles remain attached to the plastics surface (i.e., bubbles of 1 mm or lesser, where surface tension stabilizes them more effectively). We rarely observed more than one 1 mm bubble attached to the plastic sample, and never more than five 1 mm bubbles.

Relative contribution

In order to assess the relevance of the added buoyancy contributed by attached bubbles, we consider an idealized sample based on Cup_PP_100 (Fig. B1A). This idealized sample is formed by a cylinder with one cover in one end (hence, a simplistic plastic cup). The height of this idealized plastic cup is 83 mm (ℓ_{max}) and the diameter (constant across height, differently from Cup_PP_100) is 55.2 mm ($\ell_\perp$, based on Cup_PP_100 properties, see Table 2). Considering the total volume of Cup_PP_100 (Table 2) and its idealized dimensions, the mean thickness of this virtual sample corresponds to 130 μm. Considering the PP plastic density estimated with pycnometer (Table 2), and a given number of bubbles (n_b), we estimate the forces for quiescent water conditions and a static plastic element ($F_w = 0$ N) and different submergence levels (percentage of cup within the water) of a horizontal cup (i.e., axis parallel to the water surface).

The forces evaluated on the control volume are shown in Fig. B1. We observe that even for extreme, unrealistic conditions ($n_b = 25$, $d_b = 2$ mm, Fig. B1C) the effect of bubbles is smaller than any surface tension scenario considered (contact angles: 97, 105 and 115°, Fig. B1B-E). We consider here that the contact angle can yield a variable vertical projection ($\sin(\theta)$, either in the inner and outer faces of the cup (Fig. B1A). Accounting for other factors, such as the dynamic surface tension (which can be up to 40 % larger than the static one, Hauner et al., 2017), would reinforce the hypothesis that surface tension force is significantly larger than the remaining bubbles' contribution.

We also observe that the contact line (inside and outside of the cup) is reasonably insensitive to the submergence level for this plastic orientation since it is dominated by ℓ_{max}, yet in our calculations, surface tension nulls when submergence approaches 0 and 1.0 because of symmetry of forces between inner and outer faces. In reality, right before detachment from the surface, only the outer face is in contact with the free surface. We call this

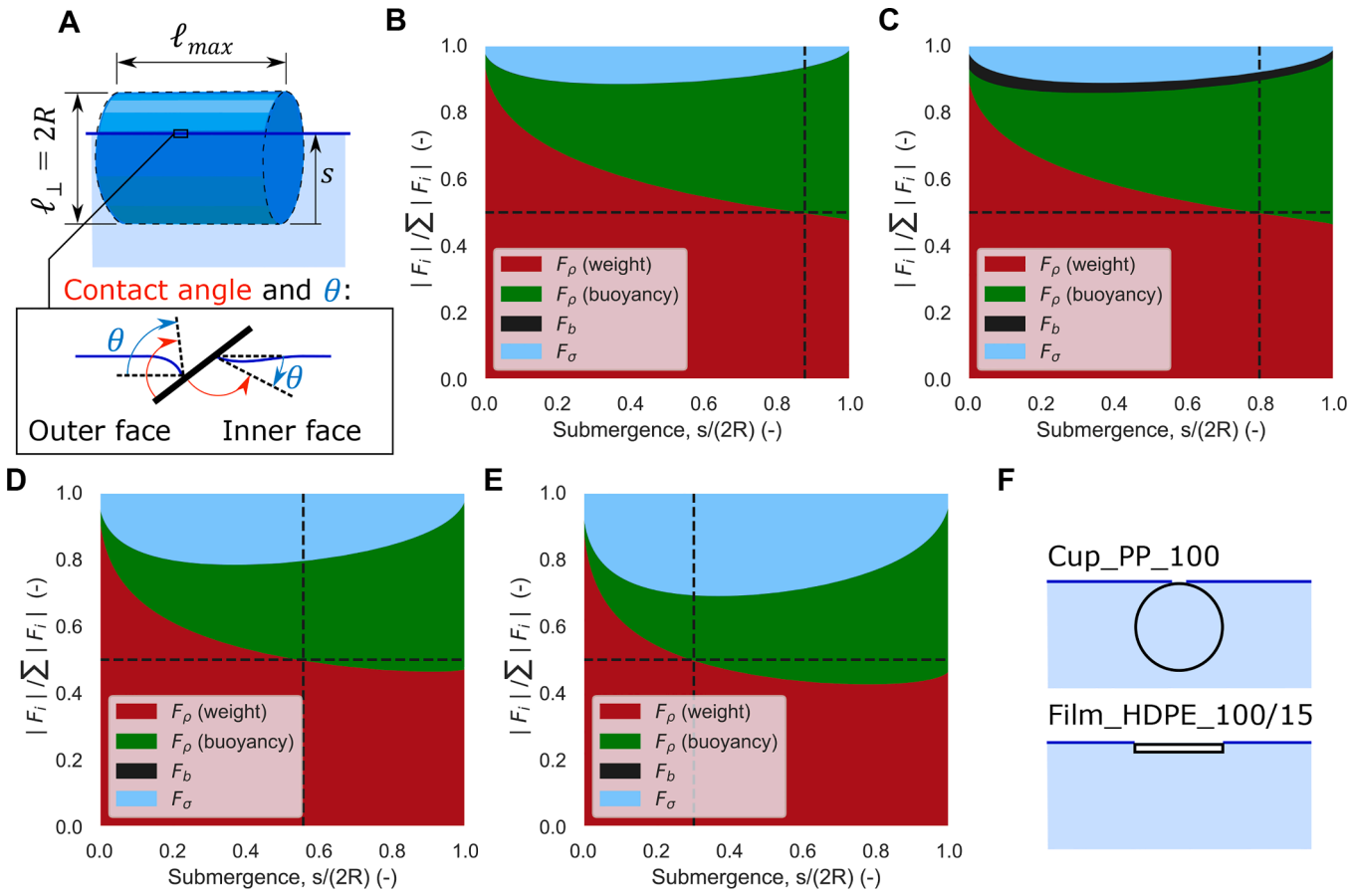

Fig. B1. Forces acting on an idealized PP cup with axis parallel to the free surface. **A** Sketch with relevant dimensions. Effect of increasing bubble count: **B** $n_b = 5$, $d_b = 2$ mm (beyond max. observed) and **C** $n_b = 25$, $d_b = 2$ mm (unrealistic). Constant bubble count ($n_b = 2$, $d_b = 1$ mm), sensitivity to different contact angles: **D** 105°, **E** 115°. **F** Sketch for the max-sigma state.

situation the maximum surface tension state (*max-sigma state*), which we analyze separately below.

Upward, positive surface tension forces represent a jump condition (escape-over-a-barrier condition, Amir, 2021) to be overcome by an extreme turbulence event. Bubbles, different from surface tension effects, would affect the plastic elements at all depths (and not only in the near free surface) thus modifying the Rouse profile from bed to surface.

Maximum surface tension state (max-sigma state)

We consider now the state of maximum surface tension (*max-sigma state*, Table B1) possible during the plastic transport experiments (Fig. B1F). For cups, this is the last contact before detachment, with only its external face in contact with the free surface (note that in Fig. B1B-E, the inner face of the cup can present downward surface tension partially compensating the outer face of the cup). For films, the max-sigma state is horizontally extended at the free surface while only the lower face is wet. The contact angles considered correspond to that of Vlaeva et al. (2012) for PP and de Luna et al. (2014) for HDPE although, in this state, the resultant does not change significantly for contact angles between 75 to 110 °, and thus is less sensitive to the material.

Table B1
Ratio of relevant forces during max-sigma state.

ID	$F_\sigma/\lvert F_\rho(\text{weight})\rvert$*	$F_\sigma/\lvert F_\rho(\text{buoyancy})\rvert$**
Cup_PP_100	0.59	0.53
Film_HDPE_100	15.62	14.97
Film_HDPE_15	56.01	53.68

* Only considers weight.
** Only considers water upthrust.

Appendix C. Water velocimetry filtering

Each ADV time series was analyzed following the protocol detailed below:

- Instantaneous velocity samples with COR < 80 % (correlation) and SNR < 10 dB (Signal-to-Noise Ratio) were filtered out (replaced by a NaN).
- A mean flow velocity was estimated for each point of the profile.
- The median misalignment of each profile (based on x and y mean velocities, $\bar{u_x}$ and $\bar{u_y}$ respectively) was estimated and then instantaneous velocity estimations were corrected (rotation to null $\bar{u_y}$). All misalignments remained below 1.9 degrees, with an average value of the absolute rotations of 0.9 degrees.
- An statistical filtering was applied to each time series, based on the Phase-Space Thresholding Method of Goring and Nikora (2002) as modified by Wahl (2003). No spike replacement was performed, but instead a NaN value was considered for the position of the outlier.
- The percentage of NaN for each u_x, u_y and u_z time series was estimated. When the maximum of these three surpassed 40 %, the point recording was discarded from the profile. Data acceptance rate are summarized in the Supplemental Material (Table S1).

Appendix D. Plastic samples properties

Main physical and geometrical properties of the plastic samples are presented in Table D1, Table D2 and Table D3.

Table D1
Sample class, material, weight and density of the plastic samples used in the hydrodynamic experiments (Fig. 3). Density estimations repeated 5 times using a pycnometer, and each test following ISO 1183-1:2019(E)(ISO, 2019); ε_ρ (%) = 100*STD/average, with STD the standard deviation.

ID	Source	Processing	Class	Material*	ρ_p (kg/m^3)	ρ_p (kg/m^3) - STD	ε_ρ (%)	M_p (g)	ε_M (%)**
Cup_PP_100	Plastic cup	Intact samples	Rigid 3D body	PP	907.33	2.3	0.25	2.09	3.75
Cup_PP_98_def	Plastic cup	Crashed by human weight, foot pressure	Damaged rigid 3D body	PP	907.33	2.3	0.25	2.04	4.07
Cup_PP_50	Plastic cup	Intact samples cut by half	Rigid quasi-2D fragment	PP	907.33	2.3	0.25	1.04	5.49
Cup_PP_05	Plastic cup	Intact samples, cut at one fourth of the perimeter	Smaller rigid quasi-2D fragment	PP	907.33	2.3	0.25	0.11	8.23
Film_HDPE_100	Supermarket plastic bag	Squared cut	Deformable film	HDPE	956.48	3.2	0.32	0.22	7.35
Film_HDPE_15	Supermarket plastic bag	Smaller, squared cut	Smaller deformable film	HDPE	956.48	3.2	0.32	0.033	27.79***
Mask****	Disposable face masks	Intact	Deformable multi-layer material	Several	-	-	-	3.05	1.50

* Material determined based on the recycling codes found in the samples and cross checked against common density range for such materials.
** ε_M includes single samples variability (STD) and balance measuring tolerance (0.01 g).
*** Single samples tolerance estimated in groups of 5 samples (i.e., variability corresponds to groups of five samples together).
**** Face masks include layers of several materials and their density was not estimated.

Table D2
Geometric properties of damaged cups (Cup_PP_98_def).

ID	Sample no.	ℓ_{max} (mm)	$\ell_\perp$ (mm)
Cup_PP_98_def	1	77	72
	2	89	83
	3	85	71
	4	88	72
	5	87	80
	6	94	73
	7	96	79
	8	88	66
	9	84	74
	10	93	69

Table D3
Rising velocity under quiescent transport conditions. Experiments are repeated three times and averaged over the equilibrium path. Minimum (min) and maximum (max) rising velocities correspond to experiments with smaller and higher velocities obtained. w corresponds to an average of the terminal velocity of the three repetitions.

ID	w (mm/s)	w (mm/s) – min	w (mm/s) – max
Cup_PP_100	26.2	23.6	30.4
Cup_PP_98_def	29.2	25.0	36.7
Cup_PP_50	18.6	16.4	20.6
Cup_PP_05	11.7	10.3	13.5
Film_HDPE_100	5.4	3.8	7.6
Film_HDPE_15	2.4	2.2	2.6
Mask	101.8	73.0	122.5

Appendix E. Statistical test for the determination of the number of samples used in the experiments

The uncertainty analysis for the suspended particles concentration included generating 1,000 synthetic experiments for each of the 85 different levels of N (sample size) considered, which varied between 10 and 1,000 samples; i.e., a total of 85,000 simulations. The inverse transform sampling method was used to draw random samples from Eq. (4). A *sample 1* with a limited N number of particles drawn was compared to a control sample with much larger number of samples (9,999 particles drawn), which is regarded as reference *true* Rouse profile. The Kolmogorov-Smirnov statistic (Fig. 5F, background) shows the maximum difference between the cumulative density functions of sample 1 and the control sample. Differences can be expected, decreasing with N as a part of the stochastic nature of the experiments. A total number of 150 samples was considered sufficient to keep uncertainty reasonable while allowing ample testing in laboratory.

Appendix F. Detected plastics statistics

The thickness of the surface transport layer is presented in Table F1 and the count per transport region in Table F2.

Table F1
Thickness of the surface transport layer a.

ID plastic	ID flow	β (-)	Γ (-)	a (cm)	a_{KS} (cm)	λ (cm)	a/λ (-)
Cup_PP_100	V1	3.00	33.75	4.41	4.15	10.79	0.41
	V2	2.00	14.94	5.23	7.96	10.79	0.48
	V3	1.44	7.77	4.51	N.A.N.	10.79	0.42
	V4	1.19	5.35	5.20	8.23	10.79	0.48
	V5	1.04	4.08	5.04	5.04	10.79	0.47
Cup_PP_98_def	V1	3.34	33.75	*	*	*	*
	V2	2.22	14.21	5.35	2.10	11.37	0.47
	V3	1.60	7.40	5.86	11.01	11.37	0.52
	V4	1.33	5.09	5.55	7.08	11.37	0.49
	V5	1.16	3.88	5.67	5.84	11.37	0.50
Cup_PP_50	V1	2.13	33.75	8.98	5.61	10.79	0.83
	V2	1.42	14.94	4.55	N.A.N.	10.79	0.42
	V3	1.02	7.77	*	*	10.79	*
	V4	0.85	5.35	4.88	N.A.N.	10.79	0.45
	V5	0.74	4.08	4.55	N.A.N.	10.79	0.42
Cup_PP_05	V1	1.34	75.06	1.32	1.15	4.82	0.27
	V2	0.89	33.23	1.52	1.46	4.82	0.32
	V3	0.64	17.29	2.36	1.20	4.82	0.49
	V4	0.53	11.90	2.34	1.42	4.82	0.49
	V5	0.47	9.07	2.83	1.31	4.82	0.59
Film_HDPE_100	V1	0.62	22.28	7.14	N.A.N.	16.64	0.43
	V2	0.41	9.86	5.10	2.03	16.64	0.31
	V3	0.30	5.13	*	*	16.64	*
	V4	0.25	3.53	6.99	19.38	16.64	0.42
	V5	0.21	2.69	6.80	19.58	16.64	0.41
Film_HDPE_15	V1	0.27	57.16	5.36	N.A.N.	6.29	0.85
	V2	0.18	25.30	3.84	8.22	6.29	0.61
	V3	0.13	13.16	3.42	1.28	6.29	0.54
	V4	0.11	9.06	3.26	N.A.N.	6.29	0.52
	V5	0.10	6.91	2.99	N.A.N.	6.29	0.47
Mask	V1	11.65	20.96	4.47	2.57	19.51	0.23
	V2	7.75	9.28	3.86	1.65	19.51	0.20
	V3	5.59	4.83	4.90	2.08	19.51	0.25
	V4	4.64	3.32	3.70	1.29	19.51	0.19
	V5	4.05	2.53	4.31	1.77	19.51	0.22

* Corrupted video. N.A.N.: not-available-number; i.e., p-value below 10^{-3} not reached.

Table F2
Number of plastic particles detected per experiment and estimated non-stationarity in the concentrations. The latter is assessed by counting differences between plastics entering the observation window in suspension and when they exit (ΔN_β, exit minus entry plane suspended plastic's counts). Δx is the average x distance travelled, between entry and exit sections in the observation window. The percentage of change per unit meter is then estimated as $100\cdot(\Delta N_\beta/N_p)/\Delta x$ (%/m).

ID plastic	ID flow	N_p (-)	N_β (-)	N_Γ (-)	$N_{\Gamma,sus}$ (-)	$N_{\Gamma,surf}$ (-)	ΔN_β (-)	Δx (m)	$100\cdot(\Delta N_\beta/N_p)/\Delta x$ (%/m)
Cup_PP_100	V1	156	3	153	0	153	0	0.29	0.00
	V2	143	21	122	9	113	0	0.23	0.00
	V3	64	33	31	1	30	4	0.22	28.21
	V4	134	75	59	16	43	3	0.33	6.83
	V5	148	94	54	24	30	-1	0.32	-2.10
Cup_PP_98_def	V1	*	*	*	*	*	*	*	*
	V2	98	17	81	4	77	4	0.22	18.59
	V3	76	38	38	5	33	2	0.21	12.53
	V4	149	91	58	3	55	7	0.32	14.54
	V5	146	84	62	14	48	5	0.32	10.69

(*continued on next page*)

Table F2 (*continued*)

Cup_PP_50	V1	136	6	130	11	119	1	0.26	2.86
	V2	118	30	88	7	81	-4	0.23	-14.63
	V3	*	*	*	*	*	*	*	*
	V4	142	70	72	35	37	-3	0.32	-6.60
	V5	129	66	63	36	27	-1	0.31	-2.54
Cup_PP_05	V1	72	5	67	30	37	-4	0.21	-26.98
	V2	75	11	64	40	24	-1	0.20	-6.58
	V3	54	20	34	9	25	1	0.30	6.27
	V4	113	61	52	12	40	-4	0.28	-12.65
	V5	110	73	37	26	11	-3	0.29	-9.34
Film_HDPE_100	V1	124	30	94	1	93	-1	0.34	-2.37
	V2	156	78	78	25	53	-1	0.31	-2.08
	V3	*	*	*	*	*	*	*	*
	V4	159	105	54	16	38	-1	0.33	-1.92
	V5	141	103	38	22	16	3	0.33	6.47
Film_HDPE_15	V1	46	36	10	2	8	1	0.27	8.16
	V2	111	67	44	6	38	7	0.31	20.30
	V3	138	90	48	6	42	-2	0.30	-4.79
	V4	107	86	21	8	13	0	0.29	0.00
	V5	100	85	15	7	8	0	0.30	0.00
Mask	V1	54	0	54	0	54	2	0.22	17.12
	V2	67	0	67	1	66	0	0.22	0.00
	V3	56	2	54	17	37	-1	0.22	-8.01
	V4	25	0	25	2	23	-1	0.26	-15.45
	V5	136	1	135	36	99	1	0.31	2.38

* Corrupted video.

Appendix G: Statistical test for the detection of the surface transport layer

In addition to the direct classification of plastic elements touching the water surface, a second method is used to identify the near-surface layer. In this layer, not all plastics are transported in suspension (β-dependent); the transport of those plastics in contact with the free surface is controlled by surface tension (Γ-dependent). To ascertain significance to the existence of a transport layer where plastics dispersion does not behave solely based on turbulence and buoyancy, we conduct a statistical test (specifically, a two-sided Kolmogorov-Smirnov (KS) test). This consists on the comparison of the observed vertical distribution of plastic elements (concentration of C.o.G.) to a reference, theoretical suspended transport profile given Eq. (4). The reference Rouse profile is estimated purely based on physical parameters (β): namely, the rising velocity of the samples (Table 2) and the shear velocity of the flow (Table 1), and hence does not correspond to a best fit calibration as in previous studies.

The KS test (KS stat, see Fig. 5F, and p-value) is iteratively applied with increasing number of samples, starting from the channel bed up to the water surface. Inside the layer defined by a_{KS}, the vertical distribution of the plastics counting in the experiments and the reference suspended profiles significantly differ (p-value $< 10^{-3}$).

Appendix H. Alternative riverine monitoring techniques and performance

When adopting Str. 4 or 8 (Table H1, or Str. C or D in the manuscript), two relevant physically-based parameters (the Rouse number β and Γ) are required, which depend on the plastic element and flow conditions. For that purpose, local hydrodynamic quantities (u_*) can be estimated based on discharge and river bed roughness (Cowger et al., 2021), whereas plastic main geometry (ℓ_{max}, $\ell_{\perp}$) needs to be determined as well as the rising velocity (w). If the rising velocity is not available, literature estimations such as those proposed by Waldschläger et al. (2020) can be used together with the density estimated based on the material type, in case of clean plastic samples (van Emmerik and Schwarz, 2020). Alternatively, optimized monitoring protocols independent of β and Γ are also presented in Table H1.

In all strategies where sampling of the suspended layer is performed, it is considered that the net would capture a layer of 10 % the water depth. This is extrapolated afterwards following different strategies (Str. 5 – 8) to the whole water column or a portion of it. The performance of each monitoring strategy is presented in Table H1 and detailed in Table H6 and Fig. H1. Optimisations of the sampling point are supported by Table H2, Table H3, Table H4 and Table H5, and a summary of the bias and uncertainty of all monitoring strategies is presented in Table H6.

Table H1
Riverine plastic monitoring strategies investigated.

Str ID	ID in manuscript	Description
Str. 1	Str. A	Count at the free surface is representative of all plastic budget: $N_p^* \approx N_{\Gamma,surf}$
Str. 2	Str. B	Visual observation of the free surface with 20 % depth visibility: $N_p^* \approx N_{\Gamma}$
Str. 3		Count at the free surface, then corrected by the expected fraction of surfaced plastics (Eq. 11): $N_p^* \approx N_{\Gamma,surf}/C_{\Gamma,surf}$
Str. 4	Str. C	Visual observation of the upper 20 % and estimation of suspension with Eqn 12: $N_p^* \approx N_{\Gamma}/(1 - C_{\beta})$
Str. 5		Count at the free surface and sampling point in suspension (uniform over the water column). Suspended transport sampled at 50 % of the water column (based on sampling point optimisation, Table H2).
Str. 6		Visual observation of the free surface with 20 % depth visibility and sampling point in suspension (uniform in the lower 80 % water column). Suspended transport sampled at 50 % of the water column (based on optimisation, Table H3).
Str. 7		Count at the free surface and sampling point in suspension (Rouse, starting at 10 % depth). Suspended transport sampled at 50 % of the water column (based on optimisation, Table H4).
Str. 8	Str. D	Visual observation of the free surface with 20 % depth visibility and sampling of a point in suspension. The sampled plastic concentration is used to inform a Rouse profile, starting at 20 % depth, then used to integrate the suspended plastic count. Suspended transport sampled at 60 % of the water column (based on optimisation, Table H5).

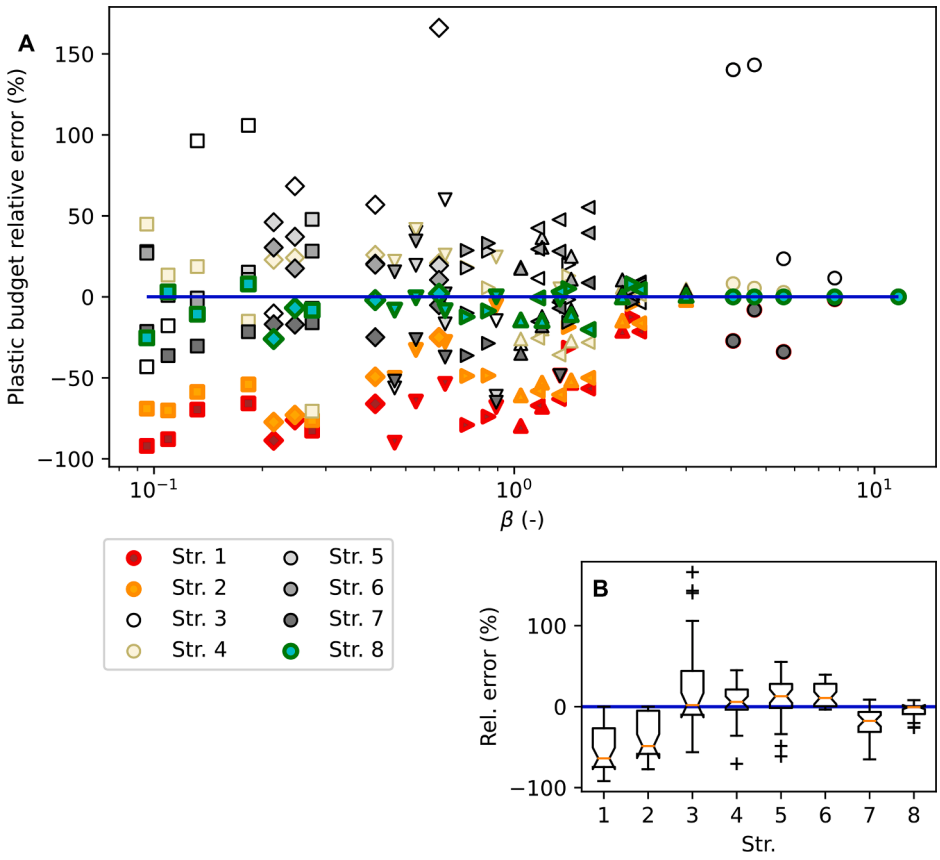

Fig. H1. Relative error on the total plastics estimation for all monitoring strategies (Str) considered (Table H1). **A** β-dependence (markers correspond to the samples of Fig. 3), **B** box whisker plot for the relative error of different strategies.

Table H2
Optimization of the sampling position of suspended transport for Str. 5 (Table H1). Sampling point at X (%) of the water column.

X (%)	r^2 (-)	Relative Mean Error (%)	Relative Median Absolute Err (%)
45	0.65	6.77	14.29
50	0.81	9.92	19.41
55	0.70	13.07	22.44
60	0.76	16.27	24.19
65	0.69	19.47	22.69
70	0.73	22.90	28.56
75	0.62	26.32	31.76
80	0.54	95.80	79.28
85	0.42	165.28	116.08
90	0.23	264.74	188.12

Table H3
Optimization of the sampling position of suspended transport for Str. 6 (Table H1). Sampling point at X (%) of the water column.

X (%)	r^2 (-)	Relative Mean Error (%)	Relative Median Absolute Error (%)
45	0.77	11.20	6.00
50	0.92	13.72	10.65
55	0.80	16.24	15.06
60	0.88	18.80	17.70
65	0.81	21.36	16.13
70	0.86	24.10	21.92
75	0.73	26.84	21.74
80	0.59	82.43	71.29

Table H4
Optimization of the sampling position of suspended transport for Str. 7 (Table H1). Sampling point at X (%) of the water column.

X (%)	r^2 (-)	Relative Mean Error (%)	Relative Median Absolute Error (%)
45	0.67	-16.06	22.30
50	0.77	-19.93	17.50
55	0.69	-23.32	25.09
60	0.71	-25.44	24.37
65	0.64	-26.99	26.52
70	0.63	-29.55	31.32
75	0.55	-32.17	34.45
80	0.64	-28.39	30.61

Table H5
Optimization of the sampling position of suspended transport for Str. 8 (Table H1). Sampling point at X (%) of the water column.

X (%)	r^2 (-)	Relative Mean Error (%)	Relative Median Absolute Error (%)
45	0.73	8.69	13.14
50	0.88	3.46	7.24
55	0.81	-1.01	8.27
60	0.93	-4.51	4.79
65	0.87	-7.14	5.90
70	0.89	-10.20	7.63
75	0.79	-13.31	12.29
80	0.85	-8.39	6.75

Table H6
Bias (Rel. Mean. Err.) and uncertainty (Rel. Median Abs. Err.) for all river monitoring strategies considered (Table H1).

	Monitoring strategy							
Performance estimator	Str. 1	Str. 2	Str. 3	Str. 4	Str. 5	Str. 6	Str. 7	Str. 8
r^2 (-)	0.16	0.25	0.41	0.73	0.81	0.92	0.77	0.93
Relative Mean Error (%)	-52.43	-36.16	22.18	3.60	9.92	13.72	-19.93	-4.51
Relative Median Absolute Error (%)	-63.84	48.71	16.24	19.25	19.41	10.65	17.50	4.79

References

ACCU DYNE TEST, 2009a. Surface Energy Data for PE: Polyethylene, CAS # 9002-88-4. Diversified Enterprises. http://www.accudynetest.com/polymer_surface_data/polyethylene.pdf.

ACCU DYNE TEST, 2009b. Surface Energy Data for PP: Polypropylene, CAS #s 9003-08-0 (atactic) and 25085-53-4 (isotactic). Diversified Enterprises. Retrieved 18/08/2022 from. https://www.accudynetest.com/polymer_surface_data/polypropylene.pdf.

Amir, A., 2021. Thinking Probabilistically: Stochastic Processes, Disordered Systems, and Their Applications. Cambridge University Press.

Andrade, H., Glüge, J., Herzke, D., Ashta, N.M., Nayagar, S.M., Scheringer, M., 2021. Oceanic long-range transport of organic additives present in plastic products: an overview. Environ. Sci. Eur. 33 (1), 1–14.

Bergmann, M., Gutow, L., Klages, M., 2015. Marine anthropogenic litter. Springer Nature.

Blanckaert, K., Lemmin, U., 2006. Means of noise reduction in acoustic turbulence measurements. Journal of hydraulic Research 44 (1), 3–17.

Bradski, G., 2000. The openCV library. Dr. Dobb's Journal: Software Tools for the Professional Programmer 25 (11), 120–123.

Cameron, S., Nikora, V., Stewart, M., 2017. Very-large-scale motions in rough-bed open-channel flow. Journal of Fluid Mechanics 814, 416–429.

Castro-Orgaz, O., 2010. Velocity profile and flow resistance models for developing chute flow. J. Hydraulic Eng. 136 (7), 447–452.

Clift, R., Grace, J.R., Weber, M.E., 1978. Bubbles, drops, and particles. Dover Publications, Inc.

Cole, M., Lindeque, P., Halsband, C., Galloway, T.S., 2011. Microplastics as contaminants in the marine environment: a review. Mar Pollut Bull 62 (12), 2588–2597. https://doi.org/10.1016/j.marpolbul.2011.09.025.

Cowger, W., Gray, A.B., Guilinger, J.J., Fong, B., Waldschläger, K., 2021. Concentration depth profiles of microplastic particles in river flow and implications for surface sampling. Environ. Sci. Technol. 55 (9), 6032–6041.

Crowe, C.T., Schwarzkopf, J.D., Sommerfeld, M., Tsuji, Y., 2012. Multiphase Flows with Droplets and Particles, 2nd ed. CRC Press.

de Luna, M.S., Galizia, M., Wojnarowicz, J., Rosa, R., Lojkowski, W., Leonelli, C., Acierno, D., Filippone, G., 2014. Dispersing hydrophilic nanoparticles in hydrophobic polymers: HDPE/ZnO nanocomposites by a novel template-based approach.

Derraik, J.G., 2002. The pollution of the marine environment by plastic debris: a review. Mar. Pollut. Bull. 44 (9), 842–852.

Dey, S., 2014. In: Rowinski, P. (Ed.), Fluvial hydrodynamics. Springer.

Duinmeijer, S.P., Moreno-Rodenas, A.M., Lepot, M., van Nieuwenhuizen, C., Meyer, I., Clemens, F.H., 2019. A simple measuring set-up for the experimental determination of the dynamics of a large particle in the 3D velocity field around a free surface vortex. Flow Meas. Instrum. 65, 52–64.

Eriksen, M., Lebreton, L.C., Carson, H.S., Thiel, M., Moore, C.J., Borerro, J.C., Galgani, F., Ryan, P.G., Reisser, J., 2014. Plastic pollution in the world's oceans: more than 5 trillion plastic pieces weighing over 250,000 tons afloat at sea. PloS One 9 (12), e111913.

Franca, M.J., Valero, D., Liu, X., 2021. Turbulence and Rivers. Reference Module in Earth Systems and Environmental Sciences. Elsevier. https://doi.org/10.1016/B978-0-12-818234-5.00135-8.

Garrido-Jurado, S., Muñoz-Salinas, R., Madrid-Cuevas, F.J., Marín-Jiménez, M.J., 2014. Automatic generation and detection of highly reliable fiducial markers under occlusion. Pattern Recognit. 47 (6), 2280–2292.

Geraeds, M., van Emmerik, T., de Vries, R., bin Ab Razak, M.S., 2019. Riverine Plastic Litter Monitoring Using Unmanned Aerial Vehicles (UAVs). Remote Sen. 11 (17) https://doi.org/10.3390/rs11172045.

Geyer, R., 2020. A Brief History of Plastics. In: Streit-Bianchi, M., Cimadevila, M., Trettnak, W. (Eds.), Mare Plasticum - The Plastic Sea: Combatting Plastic Pollution Through Science and Art. Springer International Publishing, pp. 31–47. https://doi.org/10.1007/978-3-030-38945-1_2.

Geyer, R., Jambeck, J.R., Law, K.L., 2017. Production, use, and fate of all plastics ever made. Sci. Adv. 3 (7), e1700782.

González-Fernández, D., Hanke, G., 2017. Toward a harmonized approach for monitoring of riverine floating macro litter inputs to the marine environment. Front. Mar. Sci. 4, 86.

Goring, D.G., Nikora, V.I., 2002. Despiking Acoustic Doppler Velocimeter Data. J. Hydraulic Eng. 128 (1), 117–126. https://doi.org/10.1061/(ASCE)0733-9429(2002)128:1(117).

Grossart, H.-P., Van den Wyngaert, S., Kagami, M., Wurzbacher, C., Cunliffe, M., Rojas-Jimenez, K., 2019. Fungi in aquatic ecosystems. Nat. Rev. Microbiol. 17 (6), 339–354.

Gualtieri, C., Angeloudis, A., Bombardelli, F., Jha, S., Stoesser, T., 2017. On the values for the turbulent Schmidt number in environmental flows. Fluids 2 (2), 17. https://doi.org/10.3390/fluids2020017.

Haram, L.E., Carlton, J.T., Centurioni, L., Crowley, M., Hafner, J., Maximenko, N., Murray, C.C., Shcherbina, A.Y., Hormann, V., Wright, C., 2021. Emergence of a neopelagic community through the establishment of coastal species on the high seas. Nat. Commun. 12 (1), 1–5.

Hartmann, N.B., Huffer, T., Thompson, R.C., Hassellöv, M., Verschoor, A., Daugaard, A. E., Rist, S., Karlsson, T., Brennholt, N., Cole, M., 2019. Are we speaking the same language? Recommendations for a definition and categorization framework for plastic debris. Environ. Sci. Technol. 53 (3) https://doi.org/10.1021/acs.est.8b05297.

Hauner, I.M., Deblais, A., Beattie, J.K., Kellay, H., Bonn, D., 2017. The dynamic surface tension of water. J. Phys. Chem. Lett. 8 (7), 1599–1603.
Hohermuth, B., Kramer, M., Felder, S., Valero, D., 2021. Velocity bias in intrusive gas-liquid flow measurements. Nat. Commun. 12 (1), 1–9.
ISO, 2019. Plastics—Methods for determining the density of non-cellular plastics—Part 1: Immersion method, liquid pyknometer method and titration method. ISO 1183-1: 2019(E).
Jambeck, J.R., Geyer, R., Wilcox, C., Siegler, T.R., Perryman, M., Andrady, A., Narayan, R., Law, K.L., 2015. Plastic waste inputs from land into the ocean. Science 347 (6223), 768–771.
Jenner, L.C., Rotchell, J.M., Bennett, R.T., Cowen, M., Tentzeris, V., Sadofsky, L.R., 2022. Detection of microplastics in human lung tissue using μFTIR spectroscopy. Sci. Total Environ. 831, 154907.
Kataoka, T., Nihei, Y., 2020. Quantification of floating riverine macro-debris transport using an image processing approach. Sci. Rep. 10 (1), 2198. https://doi.org/10.1038/s41598-020-59201-1.
Lebreton, L.C., Van Der Zwet, J., Damsteeg, J.-W., Slat, B., Andrady, A., Reisser, J., 2017. River plastic emissions to the world's oceans. Nat. Commun. 8 (1), 1–10.
Lechthaler, S., Waldschläger, K., Stauch, G., Schüttrumpf, H., 2020. The way of macroplastic through the environment. Environments 7 (10), 73.
Leslie, H.A., Van Velzen, M.J., Brandsma, S.H., Vethaak, A.D., Garcia-Vallejo, J.J., Lamoree, M.H., 2022. Discovery and quantification of plastic particle pollution in human blood. Environ. Int. 163, 107199.
Li, J., Zhang, K., Zhang, H., 2018. Adsorption of antibiotics on microplastics. Environ. Pollut. 237, 460–467.
Meijer, L.J., van Emmerik, T., van der Ent, R., Schmidt, C., Lebreton, L., 2021. More than 1000 rivers account for 80% of global riverine plastic emissions into the ocean. Sci. Adv. 7 (18), eaaz5803.
Napper, I.E., Davies, B.F., Clifford, H., Elvin, S., Koldewey, H.J., Mayewski, P.A., Miner, K.R., Potocki, M., Elmore, A.C., Gajurel, A.P., 2020. Reaching new heights in plastic pollution—preliminary findings of microplastics on Mount Everest. One Earth 3 (5), 621–630.
Nezu, I., Rodi, W., 1986. Open-channel flow measurements with a laser Doppler anemometer. J. Hydraulic Eng. 112 (5), 335–355.
Roberts, K.P., Phang, S.C., Williams, J.B., Hutchinson, D.J., Kolstoe, S.E., de Bie, J., Williams, I.D., Stringfellow, A.M., 2021. Increased personal protective equipment litter as a result of COVID-19 measures. Nat. Sustain. 1–8.
Rouse, H., 1961. Fluid mechanics for hydraulic engineers. Dover, New York.
Schmidt, C., Krauth, T., Wagner, S., 2017. Export of plastic debris by rivers into the sea. Environ. Sci. Technol. 51 (21), 12246–12253.
Thompson, R.C., Moore, C.J., Vom Saal, F.S., Swan, S.H., 2009. Plastics, the environment and human health: current consensus and future trends. Philosophical Transactions of the Royal Society B: Biological Sciences 364 (1526), 2153–2166.
Topouzelis, K., Papakonstantinou, A., Garaba, S.P., 2019. Detection of floating plastics from satellite and unmanned aerial systems (Plastic Litter Project 2018). Int. J. Appl. Earth Observ. Geoinform. 79, 175–183.
van der Wal, M., van der Meulen, M., Tweehuijsen, G., Peterlin, M., Palatinus, A., Kovač Viršek, M., Coscia, L., Kržan, A., 2015. Identification andAssessment of Riverine Input of (Marine) Litter.
van Emmerik, T., Kieu-Le, T.-C., Loozen, M., Van Oeveren, K., Strady, E., Bui, X.-T., Egger, M., Gasperi, J., Lebreton, L., Nguyen, P.-D., 2018. A methodology to characterize riverine macroplastic emission into the ocean. Front. Mar. Sci. 5, 372.
van Emmerik, T., Roebroek, C., De Winter, W., Vriend, P., Boonstra, M., Hougee, M., 2020. Riverbank macrolitter in the Dutch Rhine–Meuse delta. Environ. Res. Lett. 15 (10), 104087.
van Emmerik, T., Schwarz, A., 2020. Plastic debris in rivers. Wiley Interdisciplinary Reviews: Water 7 (1), e1398.
Vlaeva, I., Yovcheva, T., Viraneva, A., Kitova, S., Exner, G., Guzhova, A., Galikhanov, M., 2012. Contact angle analysis of corona treated polypropylene films. J. Phys. Conf. Ser.
Vriend, P., van Calcar, C., Kooi, M., Landman, H., Pikaar, R., van Emmerik, T., 2020. Rapid assessment of floating macroplastic transport in the Rhine. Front. Mar.Sci. 7 https://doi.org/10.3389/fmars.2020.00010.
Wahl, T.L., 2003. Discussion of "Despiking Acoustic Doppler Velocimeter Data", by Derek G. Goring and Vladimir I. Nikora. J. Hydraulic Eng. 129 (6), 484–487. https://doi.org/10.1061/(ASCE)0733-9429(2003)129:6(484).
Waldschläger, K., Born, M., Cowger, W., Gray, A., Schüttrumpf, H., 2020. Settling and rising velocities of environmentally weathered micro- and macroplastic particles. Environ. Res. 191, 110192 https://doi.org/10.1016/j.envres.2020.110192.
Waldschläger, K., Brückner, M.Z.M., Carney Almroth, B., Hackney, C.R., Adyel, T.M., Alimi, O.S., Belontz, S.L., Cowger, W., Doyle, D., Gray, A., Kane, I., Kooi, M., Kramer, M., Lechthaler, S., Michie, L., Nordam, T., Pohl, F., Russell, C., Thit, A., Umart, W., Valero, D., Varrani, A., Warrier, A.K., Woodall, L.C., Wu, N., 2022. Learning from natural sediments to tackle microplastics challenges: a multidisciplinary perspective. Earth-Sci. Rev. 228, 104021 https://doi.org/10.1016/j.earscirev.2022.104021.
Waldschläger, K., Schüttrumpf, H., 2019. Effects of Particle Properties on the Settling and Rise Velocities of Microplastics in Freshwater under Laboratory Conditions. Environ. Sci. Technol. 53 (4), 1958–1966. https://doi.org/10.1021/acs.est.8b06794.
White, F.M., 2006. Viscous Fluid Flow. McGraw-Hill.
White, F.M., 2016. Fluid Mechanics, 8th ed. McGraw Hill.
Zaat, L.I., 2020. Below the surface: A laboratorial research to the vertical distribution of buoyant plastics in rivers. Delft University of Technology (MSc. thesis).